CHARACTERIZATION OF A SINGLE PHOTON SENSING AND PHOTON NUMBER RESOLVING CMOS DETECTOR FOR ASTROPHYSICS

M.S. *Master of Science*

in Astrophysical Sciences and Technology

Justin P. Gallagher

School of Physics and Astronomy

Rochester Institute of Technology

Rochester, New York

August 2020

ASTROPHYSICAL SCIENCES AND TECHNOLOGY
COLLEGE OF SCIENCE
ROCHESTER INSTITUTE OF TECHNOLOGY
ROCHESTER, NEW YORK

CERTIFICATE OF APPROVAL

M.S. DEGREE THESIS

The M.S. Degree Thesis of *Justin Gallagher* has been examined and approved by the thesis committee as satisfactory for the thesis requirement for the M.S. degree in Astrophysical Sciences and Technology.

Dr. Donald F. Figer, Committee Chair and Thesis Advisor

Dr. Michael Zemcov, Committee Member

Dr. Gregory Howland, Committee Member

Date _____

Characterization of a Single Photon Sensing and Photon Number Resolving CMOS Detector for Astrophysics

By

Justin Gallagher

A thesis submitted in partial fulfillment of the requirements for the degree of M.S. in Astrophysical Sciences and Technology, in the College of Science, Rochester Institute of Technology.

August, 2020

Approved by

Dr. Andy Robinson	Date
Director, Astrophysical Sciences and Technology	

Abstract

Next-generation NASA missions, such as the LUVIOR and HabEx concepts, require single photon counting large-format detectors. Charge Coupled Devices (CCDs) have typically been used for optical applications in similar flagship missions of the past. CCDs have excellent properties in most metrics but have their own challenges for single photon counting applications. First, typical CCDs have a read noise of a few electrons, although recent modifications (EMCCDs) use an on-chip gain to amplify the signal above the read noise. Secondly, the signal is carried by charge that is transferred across the detector array. While CCDs for NASA missions are carefully fabricated to minimize defects, continuous bombardment from high energy radiation in space will damage the detector over the lifetime of the mission. This will degrade the charge transfer efficiency and in turn, reduce the single photon counting ability of the CCD. CMOS devices offer a different architecture that mitigates some of these problems. In CMOS image sensors, each pixel has its own charge to voltage converter and in-pixel amplifier mitigating issues found with charge transfer efficiency. Additional circuits that are critical to operation of the sensor can be incorporated on chip allowing for a parallel readout architecture that increases frame rate and can decrease read noise.

This thesis is a collection of work for the characterization of a room temperature characterization, low-noise, single photon counting and photon number resolving CMOS detector. The work performed in this thesis will provide the framework for a technology development project funded by NASA Cosmic Origins (COR) program office. At the end of the two-year project, a megapixel CMOS focal plane array will be demonstrated to satisfy the stated needs of the LUVOIR and HabEx future astrophysics space mission concepts with a launch date near the 2040s.

Acknowledgements

Image sensor technology is one of the most fundamental and interesting fields of modern technology. Digital image sensors are based on some of the most influential discoveries since the turn of the 1900s. To perform research on scientific image sensors for astrophysical observations and NASA missions, in my opinion, is equivalent to a child's first time at an amusement park. I cannot thank the Astrophysical Sciences and Technology program enough, as they have provided the BS/MS opportunity to make such an impact on future technology so early on in my career. Opportunities like this can significantly direct the passion and work that motivates students to move forward towards their dreams.

Dr. Donald F. Figer has been more of a mentor than I could hope for. Not only has Don provided an image sensor to perform a thesis on, the laboratory space and equipment to do so, Don has been a fantastic influence on the conduct of my professional career. Don's background comes directly from some of the most influential NASA missions such as the Hubble Space Telescope, Large Synoptic Survey Telescope (LSST) guider system, and the James Web Space Telescope (JWST) to name a few. As a renowned detector scientist, Don pushes his students to perform to the best of their ability and has the same expectations as any organization related to imaging sensors and space missions. Furthermore, Don's acceptance for me to work under his guidance has provided numerous opportunities that go beyond the classroom that most graduate students would dream of. I have presented a poster at the 9th Single Photon Workshop in Milian, Italy, an international conference where I was able to talk with the leading experts from many renown institutions and organizations from around the world. I was sent to Gigajot Technology, Inc. for a week to work alongside some of their engineers and help develop my understanding of the image sensor characterized in this thesis. I was able to meet and collaborate with Dr. Eric R. Fossum, the primary inventor of the CMOS active pixel image sensor "camera on a chip", a critical technology found in every commercial cellphone. Most important to my professional career, Don has chosen me to manage the NASA funded two-year project and has offered me a position as Lab Engineer I at the Center for Detector.

While I cannot thank Don enough, it is clear that Don has fueled the opportunity for my astrophysics dream as a young high schooler to develop into my career.

I thank my parents, Brian and Lynn, for encouraging me to continue my education and supporting me in my personal and academic endeavors. Finally, I thank my sister, Shannon, for being the older child and the ensuing sibling rivalry that has constantly pushed me to go further.

Contents

List of Figures

List of Tables

Acronyms

ADC Analog to Digital Converter

ADU Analog to Digital Unit

APS Active Pixel Sensor

ASIC Application Specific Integrated Circuit

ATLAST Advanced Technology Large Aperture Space Telescope

BSI Back Side Illuminated

CCD Charge Coupled Device

CDS Correlated Double Sampling

CEB Cold Electronics Board

CfD Center for Detectors

CIS CMOS Image Sensor

CMOS Complementary Metal Oxide Semiconductor

COR Cosmic Origins

CVF Charge to Voltage Factor

EMCCD Electron Multiplying Charge Coupled Device

FD Floating Diffusion

FET Field Effect Transistor

FOV Field of View

FPGA Field Programmable Gate Array

FPS Frames Per Second

HABEX Habitable-Exoplanet Imaging Mission

HDI High Definition Imager

IDL Interactive Data Language

IR Infrared

JFET Junction Field Effect Transistor

JPL Jet Propulsion Laboratory

LSB Least Significant Bit

LUVIOR Large Ultraviolet Optical Infrared Surveyor

MOSFET Metal Oxide Semiconductor Field Effect Transistor

NASA National Aeronautics and Space Administration

NIR Near-Infrared

NUV Near-Ultraviolet

PCB Printed Circuit Board

PD Photodiode

PPD Pinned-Photodiode

PSF Point Spread Function

QE Quantum Efficiency

QIS Quanta Image Sensor

QISPF Quanta Image Sensor Pathfinder

QTH Quartz Tungsten Halogen

RIT Rochester Institute of Technology

SAT Strategic Astrophysics Technology

SF Source Follower

SNR Signal to Noise Ratio

SPAD Single Photon Avalanche Diode

SW Storage Well

TPG Tapered Pump Gate

TRL Technology Readiness Level

TX Transfer Gate

UVIS UV-visible

Chapter 1

Introduction

This thesis is a collection of work that characterizes a single photon sensing and photon-number-resolving CMOS image detector array called a quanta image sensor (QIS). A team of graduate and undergraduate students at Dartmouth University led by Dr. Eric Fossum designed the QIS. The QIS chip is integrated in a commercially produced camera system with off-chip electronics by Gigajot Technology, Inc., a company started by former Dartmouth PhD students to commercialize QIS technology. In this thesis, the camera system is referred to as the QIS Pathfinder (QISPF).

The NASA Astrophysics Visionary Roadmap [1] identifies the long-term astrophysics goals and program plans over the next three decades. One goal is to develop a large space telescope with improvements in sensitivity, spectroscopy, high contrast imaging, astrometry, angular resolution and/or wavelength coverage as a possible post-WFIRST surveyor-class facility. Enduring Quests and Daring visions outlined multiple future concept missions, some of which would benefit from developing the technology in this thesis. As such, this thesis will serve as a preliminary investigation for a larger research project funded by the NASA Cosmic Origins (COR) program office under a Strategic Astrophysics Technology (SAT) grant.

1.1 Photodetector Background

Image sensors work using semiconductors that absorb photons, the discrete quanta of light. Photons must have an energy greater than the semiconductors band-gap, defined as the energy difference between the valance and conduction bands. The photon is absorbed and perturbs a valance band electron into the conduction band. The electron freely drifts in a random walk unless it is forced by an electric field to migrate. When fabricating a sensor, impurities are added to the bulk material of the semiconductor specifically to shape the electric field [2]. This is known as doping. After fabrication, an external electric field controls the migration of charge carriers in an image sensor. All complementary metal-oxide semiconductor (CMOS) image sensors perform the same basic functions listed below and demonstrated in figure 1.1:

1. generate and collect charge carriers
2. convert the charge carriers into a signal of voltage or current
3. measure and record the signal

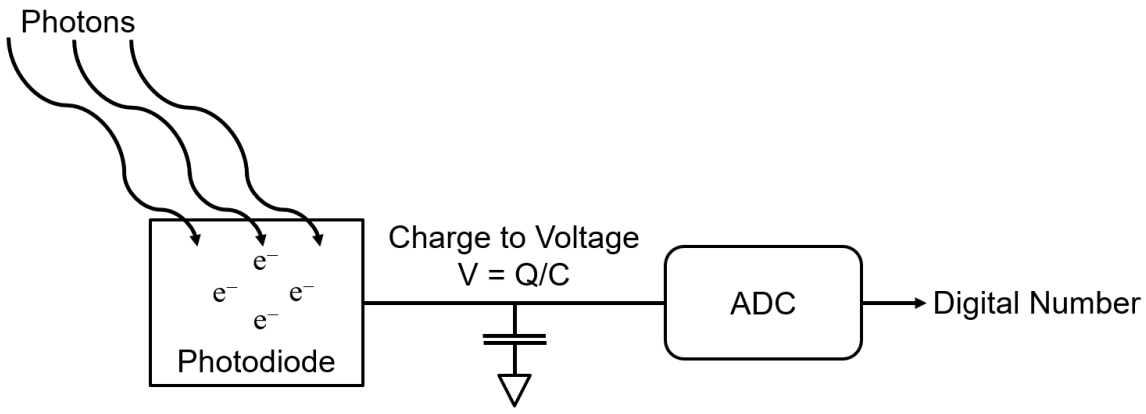

Figure 1.1: basic schematic of functions for a digital camera

The CMOS image sensor (CIS) is a semiconductor device used for making digital cameras. In a digital camera, charge carriers are generated and collected in a semiconductor. Integrated

circuits convert charge carriers into an analog signal. An analog-to-digital converter (ADC) converts the analog signal into a digital number where an image is created from the digitized signal from all pixels.

CMOS image sensors are mixed signal circuits that integrate a wide variety of components to perform the desired image acquisition. Components include: pixel arrays, analog signal processors, analog-to-digital converters, polarization generators, timing generators, and digital logic.

The basic architecture for a pixel was proposed by Weckler in 1967 [3]. Weckler described and analyzed a p-n junction with a reverse voltage [4]. Modern image sensors still use concepts of the p-n junction for photon detection. Shortly after, in 1968, Peter Noble described the CMOS active pixel sensor (APS).

The first APS with intra-pixel charge transfer was invented at the NASA Jet Propulsion Laboratory (JPL) in 1992-1993 and further developed at JPL and then the JPL-spinoff Photobit starting in 1995 [5] [6] [7]. Compared to charge coupled devices (CCD), CMOS image sensors consume less power, are cheaper to manufacture, and can be designed with very small form factor [8]. They are also known to have lower read noise their CCDs counterparts, however, recent work has identified areas where CCDs can futher improve this metric [9]. Occasionally referred to as the "camera-on-a-chip", CMOS image sensors quickly dominated the commercial market for image sensors in the 1990s. In 2018, over 5.5 Billion CMOS image sensors were manufactured and are found in every commercialized phone-camera [10].

1.2 The p-n Junction and Photodiode Pixel

When a photon strikes a semiconductor, if the photon has more energy than the bandgap of the semiconductor, it generates an electron-hole pair as a charge carrier. To prevent the recombination of the charge carrier and the subsequent loss of information, the semiconductor is carefully fabricated to minimize defects and locations where the the signal can become trapped.

Semiconductors are fabricated from doping a bulk material, such as silicon, with impurities

to create p-type or n-type semiconductors within the bulk material [11]. A p-type semiconductor is an extrinsic semiconductor in which the element used for doping contains one less valance electron than the bulk material. Typically, boron is used for silicon semiconductors. Boron contains one less valance electron than silicon leaving an empty bond (hole) in the atomic lattice. The hole will readily accept electrons that are free flowing. An n-type semiconductor is created by doping silicon with an element containing an extra valance electron such as phosphorus. The extra valance electron does not bond as all vacancies with silicon are filled. The extra electron becomes weakly bound in the phosphorus valance band where it can easily provide an extra electron to the conduction band when perturbed.

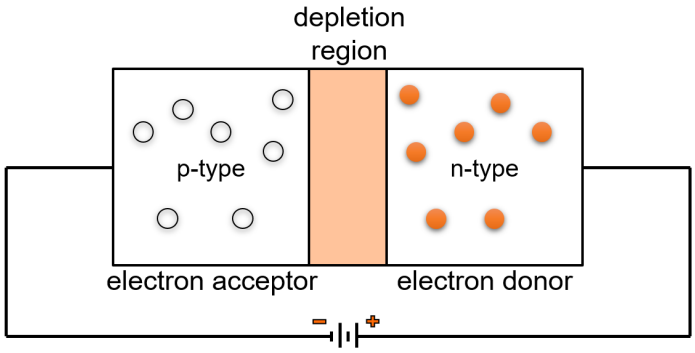

Figure 1.2: depletion region located at the p-n junction connected to an external voltage source

A p-n junction is created at the interface between a p-type and n-type material where the excess electrons of the n-type will flow as a current to fill the open bonds (holes) of a p-type material (figure 1.2). Current will stop flowing when the potential difference of the junction increases high enough, creating a depletion region. A depletion region is the region in a semiconductor device that is devoid of free electrons and holes. An external applied voltage can increase or decrease the size of the depletion region at the junction and controls the current flow of the p-n junction as a diode [12]. Under forward-bias, the depletion region will shrink and can allow a current to flow across the junction. Under reverse-bias, the depletion region grows in size and ideally no current flows across the junction up to the breakdown voltage of the diode.

For image sensors, p-n junctions are used with a reverse bias voltage [13]. Today, the p-n junctions have undergone a significant amount of development. Many varieties of diode are in use in a variety of applications. In addition to this, the PN junction forms the basis of much of today's semiconductor technology where it is used in transistors, FETs, and many types of integrated circuit. The pinned photodiode (PPD) is a variation in photodetector structure with a large depletion region. The PPD is known for its low noise, low dark current and high quantum efficiency [14].

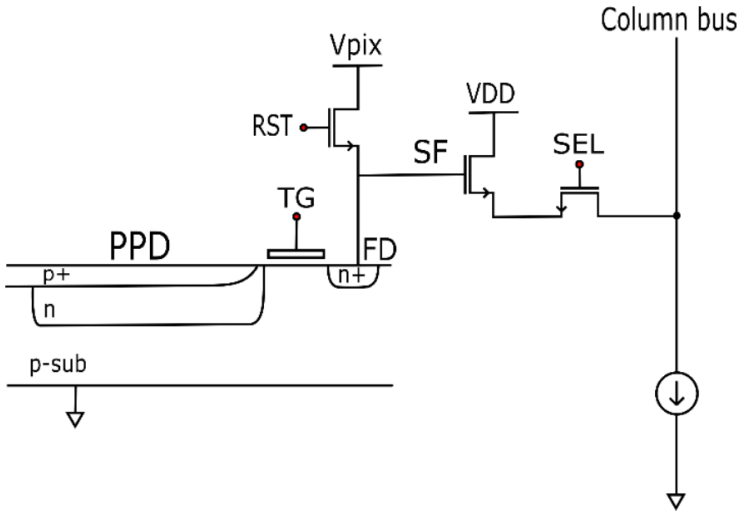

Figure 1.3: schematic of CMOS 4-Transistor active pixel sensor with pinned photodiode (PPD), transfer gate (TG), floating diffusion (FD), reset gate (RST), source follower (SF), and pixel selection (SEL) [15]

When a reverse-bias p-n junction is exposed to light, charge carriers resulting from absorbed photons collect in the depletion region. After a desired time, the collected charge carriers are converted into a voltage. In the CMOS APS design (figure 1.3), the charge to voltage conversion occurs in an in-pixel buffer known as a source follower (SF) implemented in the pixel. The capacitance sense node of the SF controls the voltage response from a charge (equation 1.2.1 and figure 1.1). The voltage response (V) on the sense node is proportional to the transferred charge (Q) and inversely proportional to the capacitance (C).

$$V = \frac{Q}{C} \tag{1.2.1}$$

An ADC digitizes the output the voltage of the SF. Gain can be applied to the voltage before the ADC. Gain increase the signal before additional electronic noise is applied, thus, increasing the signal-to-noise ratio (SNR).

1.3 The QISPF camera system

Figure 1.4: QISPF camera system

The QISPF integrates the QIS chip into a chip carrier, shown in figure 1.4, mounted on a printed circuit board (PCB) that contains off-chip electronics. The PCB is stacked at the top of three additional PCBs, one of which is an Opal Kelly XEM-7310-A75 containing a Xilinx Artix-7 field-programmable gate array (FPGA). A computer uploads a compiled configuration

file to the FPGA with the programming to control the clocking of the camera system. The XEM7310 utilizes a high transfer rate USB3 which enables quick configuration and rapid data transfer.

1.4 The Quanta Image Sensor

The QIS is a concept for a CMOS image sensors that operates like a photographic film plate that can be scaled to gigapixel formats [16]. The concept from 2005 proposed a a single-photon sensing image sensor that achieves sufficient sensitivity to achieve single-photon sensing by containing sub-diffraction pixels connected to a binary 1-bit ADC [17]. Active research began in 2008 at Samsung [18] but was short lived due to economic pressure in that period. Research began anew at Dartmouth in 2011 [19] and was supported from 2012 to the present by Rambus, Inc.

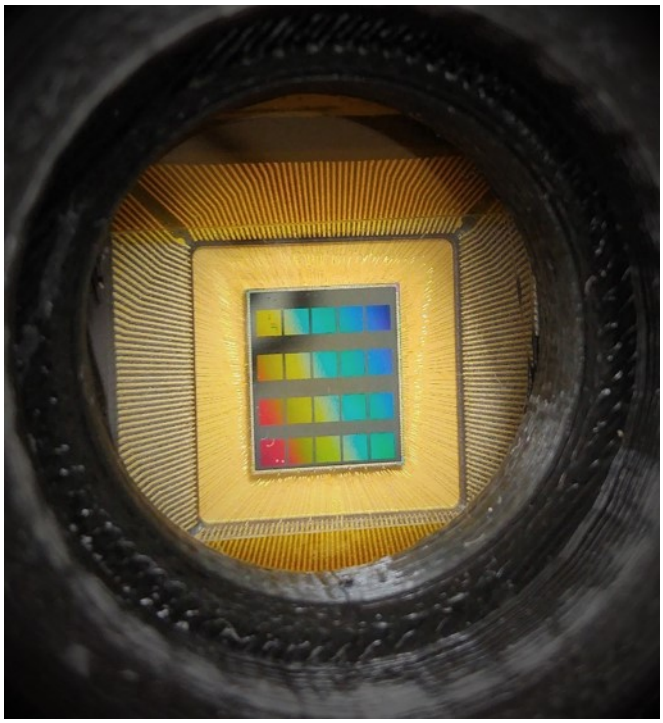

Figure 1.5: twenty QIS detectors (rainbow squares) wire-bonded (gold) in chip carrier packaged in QISPF camera housing (black edge)

Similar to the resolution element of a photographic plate, a photon will change the 1-bit

state of a resolution element. For the QIS pixel, an output digital value of zero corresponds to no photons and a one corresponds to a measured photon [20]. In order to prevent prevent saturation of a 1-bit from multiple collected charge carriers, the QIS must be read out at a rate comparable to the random photon arrival time. In concept, an image would be constructed from a stack of multiple frames read out by the device and processed by a de-noising algorithm [21].

The QISPF integrates a prototype "Pathfinder" QIS chip. The chip contains twenty prototype QIS megapixel detectors, each with slight variations in the pixel design 1.5. The twenty detectors are arranged in two main categories: detectors with a 1-bit ADC integrated on chip (Digital QIS) and detectors that utilize an off chip 14-bit ADC (Analog QIS). Within each of the two categories are sub-groups that contain variations of the SF dimensions and design (MOSFET vs JFET) and the reset gate design.

1.4.1 The QIS Pixel

The QIS pixel architecture produces a charge to voltage factor of >350 nV/e$^-$ from developing a pixel with a small sense node capacitance [22] and is shown in figure 1.6. A tapered pump-gate (TPG) reset reduced overlap and stray capacitance in the design of pixel. The pump-gate approach has been described in detail and validated in [23] [24]. To further improve performance for deep sub-electron read noise, a QIS device with a JFET SF was modeled and developed in [25] but is not the focus of this work.

Photons enter through the back side of the device (bottom of figure 1.6). The semiconductor absorbs the photon resulting in charge carrier. Ideally, all charge carriers collect in the SW but is not always true. When a photodiode transfer gate (TX) is pulsed, collected charge in the n-doped storage well (SW) transfers to the FD where a buried-channel MOSFET SF connects the FD to a multiplexing unit. The SF has a width of 0.18 µm and a length of 0.23 µm.

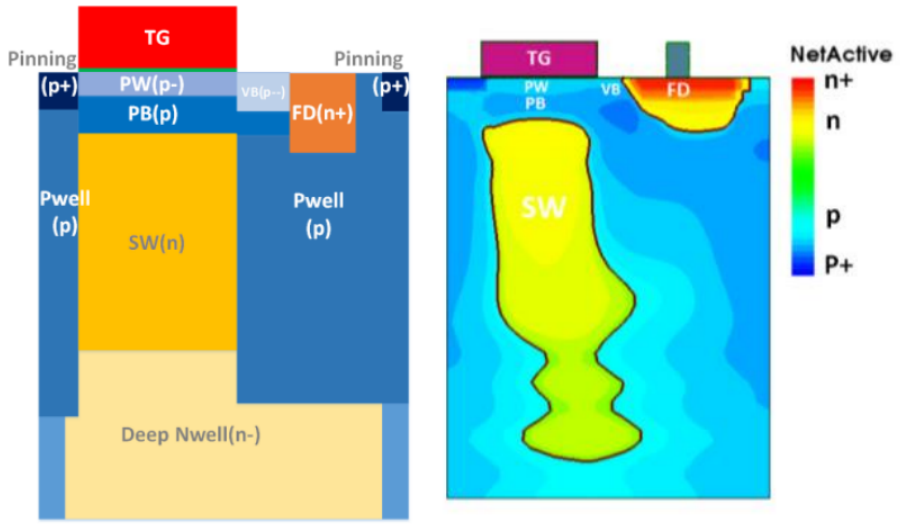

Figure 1.6: Schematic of (left) pump gate pixel doping and (right) TCAD simulation [26]

1.4.2 The Detector Array

Parameters of the detector array and pixel can be found in table 1.1. The detector has two vertically stacked substrates that are electrically connected [27]. A 45 nm backside illuminated (BSI) CMOS image sensor process fabricates the photodiode pixels on the top detector substrate. The application-specific integrated circuit (ASIC) bottom substrate contains the readout and addressing circuits. A 65 nm CMOS image sensor process is used to fabricate the ASIC substrate.

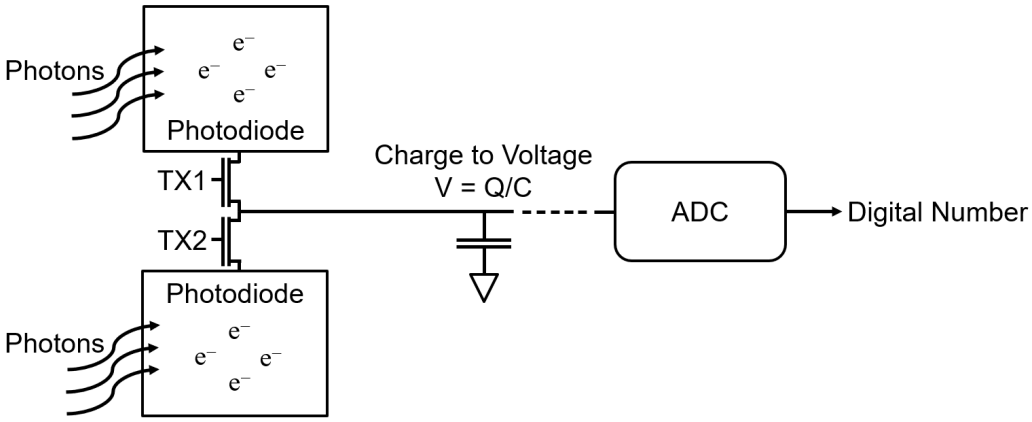

Figure 1.7: simplified two-way shared architecture with TX1 and TX2 sharing an output

The detector is a 1024(H) x 1024(V) array of pixels. The detector array is sectioned into a 4(H) x 16(V) grid where each section will be referred to as a cluster [28]. Each cluster contains 256(H) x 64(V) pixels and contains a dedicated readout circuit to output analog signal. Sixteen output pads will simultaneously readout the detector array using sixteen off-chip 14-bit ADCs. This design allows a row of 4 clusters to share a single output pad.

Pixels share a floating diffusion (FD) in a two-way shared 1(H) x 2(V) architecture (figure 1.7) [29] [30]. More accurately, two photodiode transfer gates (TX1 and TX2) share a FD and can be pulsed simultaneously or sequentially. When TX1 and TX2 are pulsed simultaneously, the charge from the two photodiodes is binned, operating as a 1024(H) x 512(V) image sensor with an effective pixel area twice as large. In this mode of operation, the integration time for the two photodiodes is the same but TX1 and TX2 are reset out of phase. To do this, the reset gate is pulsed high for a time equal to the time required to perform a set of signal samples ($\approx 10 - 34$ µs) (signal samples are described in section 1.5). During the first µs of keeping the reset gate high, TX1 is reset while TX2 is reset in the last µs.

Table 1.1: QISPF parameters

Parameter	Value
Detector Array	1024(H) x 1024 (V)
CIS Process	45 nm (pixel substrate), 65 nm (ASIC substrate)
VDD	1.8 V (Analog Array), 3 V and 2.2 V (I/O pads)
Pixel Type	BSI Tapered Pump Gate with 2-way shared readout
Pixel pitch	1.1 µm
BSI Fill Factor	100%
Charge to Voltage Factor	495 µV/e^-
Frame Rate	0.6 fps to 9.8 fps
ADC Resolution	14-bit
Output FITS Frame Size	2bytes x 1024 x 1024 = 2.1 MB
Data Rate	1.26 MB/s to 20.6 MB/s
Sampling Rate	526 kHz
Source Follower Type	Buried Channel MOSFET (0.23 µm length, 0.18 µm width

1.4.3 From Photon to Digital Image

The pixel starts with a pulse of the FD reset gate and TX to reset the FD and the photodiode. The photodiode begins integrating charge at the end of the reset pulse. Photons illuminate the "backside" of the CMOS chip and generate photoelectrons. The photo-generated electrons collect in SW with a capacity to store up to approximately 200 electrons [31].

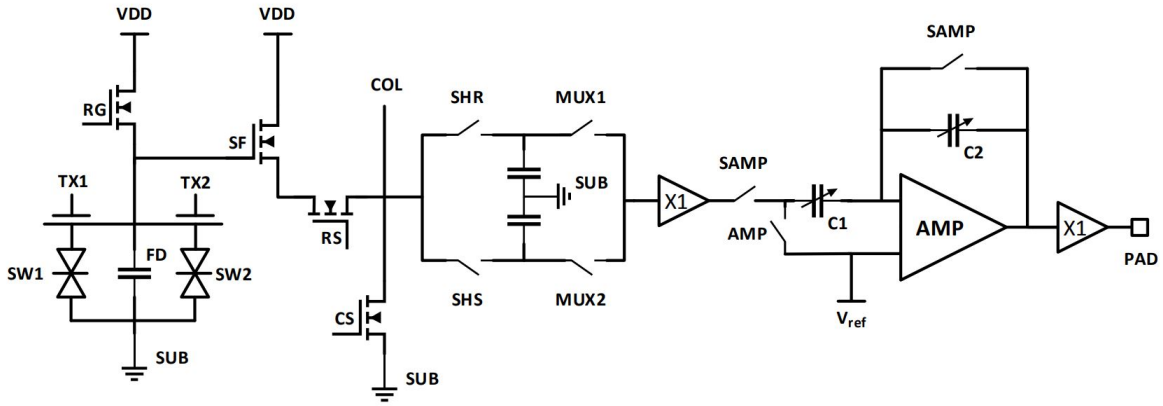

Figure 1.8: A schematic of read out signal chain for analog output [32]. The charge collected by the PPD is transferred to a floating diffusion (FD) whose voltage is monitored by a source-follower (SF) within the pixel. The FD is reset by transistor reset signal (RST) prior to transfer and the source-follower is connected to the column bus line (COL) using a row-select transistor (SEL).

An integrated circuit connects the FD to an off-chip ADC located after PAD (figure 1.8). Near the end of the integration time, but immediately before the transfer of integrated charge, the ADC performs the reset samples of the floating diffusion. The ADC samples the reset voltage a select number of times (2,4,8,16) and digitizes the measured signal each sample. The XEM7310 averages the digitized reset samples and stores the value in the on-board buffer memory. Following this, TX is pulsed high to transfer charge. The TX voltage pulse pulls the photoelectrons from the SW to the front-side surface of the device. When TX returns to a lower voltage, the electric potential "pumps" the photoelectron charge to the FD causing a change in the FD voltage. When transferred, a saturated pixel of approximately 200 electrons corresponds to a negative FD voltage change of 70-100 mV from the reset voltage. The ADC measures and digitizes the new FD voltage signal a select number of times. The FPGA averages

the signal samples, and stores the digital value. The XEM7310 sends the average reset and signal sample for a pixel to the computer in a 32-bit stream. The first 16-bits corresponds to the average reset sample and the last 16-bits corresponds to the average signal sample. IDL procedures read the raw data of the average reset and signal sample and performs correlated double sampling (CDS) subtraction. After subtraction, the IDL procedure performs image deinterlacing, where the one-dimensional data is arranged into a two-dimensional frame. The frame is saved into a flexible image transport system (FITS) file. A user can choose to not perform CDS subtraction in the IDL procedure. With this choice, the final frame of data will include the average reset or average signal sampled for each pixel depending on the users choice.

The data acquisition pipeline produces a three-dimensional flexible image transport system (FITS) [33] data cube (x, y, t) where x and y correspond to the effective size of the detector array. The value for x is always 1024 pixels, however, y changes from 512 pixels to 1024 pixels if TX1 and TX2 occur simultaneous or sequentially. The value for t corresponds to the number of captured frames. In data reduction, the frames can be stacked into an image or analyzed individually.

1.5 Correlated Double Sampling

CDS is a method to remove a fixed pattern noise when measuring electrical values such as voltages or currents. In image sensors, CDS will remove the reset noise, or kTC noise, generated by the capacitance of the FD undergoing reset [34]. The reference voltage of the pixel (i.e., the pixel's voltage after it is reset) is subtracted from the signal voltage of the pixel (i.e., the pixel's voltage at the end of integration) at the end of each integration period. This is necessary for photon number resolution of the QIS as the reset noise is larger than the voltage response from a single photoelectron. The CDS method for the QISPF is different from typical detectors. The reset samples occur directly before the transfer of integrated charge rather than right after the reset of the pixel (figure 1.9). The QISPF will average multiple reset samples and subtract the average of multiple signal samples (equation 1.5.2), however, the QISPF will

perform an extra reset and signal sample because charge is transferred at the same time as the first signal sample. The very first reset and signal sample is not used in calculating the average of samples. The time between reset samples and signal samples corresponds to the time to transfer charge.

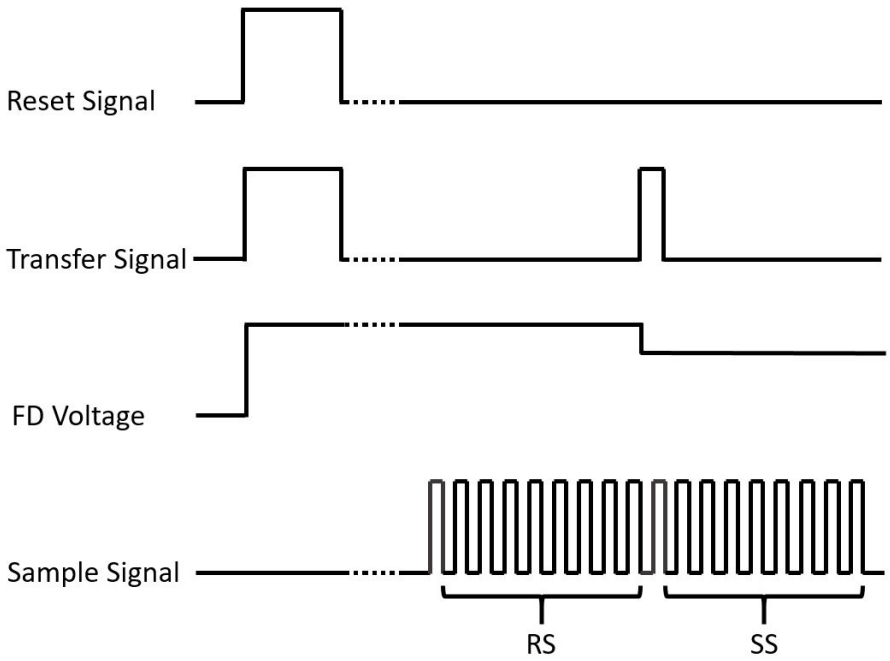

Figure 1.9: QISPF sampling diagram with reset sampling (RS) and signal sampling (SS)

$$S = \overline{RS} - \overline{SS} \tag{1.5.2}$$

where S is the signal after CDS, $\overline{RS}$ is the average of the reset samples and $\overline{SS}$ is the average of the signal samples. Transferred electron charge causes the voltage of the FD to decrease, thus, signal is subtracted from reset.

1.6 The IDL Test Suite Software

The Center for Detectors (CfD) uses data acquisition and reduction pipeline consisting of IDL procedures. To integrate the QISPF, I modified the CfD pipeline and added new IDL

procedures. The procedures use a custom-built `IDL/C/C++` driver and the `C++` Opal Kelly application programming interface to control the QISPF camera system. The IDL procedures are responsible for the following actions:

1. establish connection to the XEM7310
2. configure the FPGA
3. initialize the electronics
4. read out multiple frames of data
5. save data into a data-cube

Gigajot provided multiple compiled configuration bit files. The FPGA is configured with one configuration file at a time. The configuration file controls the clocking of the QISPF. The clocking controls the frame rate, or frames per second (FPS). The frame rate is 0.6 - 9.6 FPS. The data-cube is three dimensional with dimensions of (xpix, ypix, nframe).

Chapter 2

The Strategic Astrophysics Technology Project

My work in this thesis presents a preliminary room temperature characterization that validates published characterization metrics, supports the design of cryogenic, down to 150 K, and vacuum safe hardware, and generates requirements for the NASA funded project. Some results in this thesis were presented at the 2019 Single Photon Workshop in Milan, Italy and the 235th Meeting of the American Astronomical Society in Honolulu, Hawai'i. The following sections will outline why future NASA missions will benefit from the technology in this thesis and the work included in the SAT project.

2.1 NASA Missions: The Next Generation

Single photon counting large-format detectors will be a key technology for the future NASA Astrophysics missions such as the LUVIOR and HabEx mission concepts. This technology will have significant impact on general astrophysics, next-decade flagship NASA missions, and future Earth Science space missions. The NASA Cosmic Origins (COR) program office has funded a Strategic Astrophysics Technology (SAT) project to characterize and demonstrate the additional QIS at CfD. Donald F. Figer (principal investigator) leads the project in conjunction with Eric R. Fossum and Michael B. Zemcov (co-principal investigators).

There are several important potential benefits for NASA in pursuing CMOS-based QIS detectors for space missions: photon counting capability, large formats, relative immunity to radiation [35] [36], low power dissipation, low noise, and small form factor for a lower mass and space for more robust electronics. A next-generation space mission containing such a detector array is needed to help answer fundamental questions such as:

1. How did we get here?

2. Does life exist on nearby Earth-like exoplanets?

3. How did the universe originate and evolve to produce the galaxies, stars, and planets we see today?

2.1.1 Large UV-Optical-IR (LUVIOR) Surveyor

LUVIOR team has baselined a multi-gigapixel CMOS focal plane known as the High Definition Imager (HDI) [37]. At the specified plate scale, tiling a square degree field with tens of micron-class pixels would lead to a 4.5 m x 4.5 m focal place. With smaller pixels the optics could be significantly more compact resulting in two designs for a telescope diameter of 15 m (LUVIOR-A) and 8 m (LUVIOR-B). The HDI is a wide-field imaging camera with a 3' x 2' field of view (FOV) and a wavelength coverage of 200 - 2500 nm. The total wavelength coverage is sectioned into two channels: a NUV-visible channel (UVIS) covering 200 – 1000 nm and an NIR channel covering 1000 – 2500 nm. The UVIS would utilize a mosaic of CMOS image sensors that Nyquist sample the point-spread function (PSF) at 500 nm. The estimated systematic limit for astrometric precision is 0.34 μas (LUVIOR-A) and 0.65 μas (LUVIOR-B) in single-epoch imaging.

The Advanced Technology Large Aperture Space Telescope (ATLAST) mission concept baselines a similar implementation of a LUVIOR surveyor [38] [39]. The photon counting performance of the QIS would accommodate the demanding spectroscopy for an exoplanet biomarker program which requires a background of less than 0.001 e^-/s/pix [40].

2.1.2 A Habitable-Exoplanet (HabEx) Imaging Mission

A next-decade flagship NASA mission to image exoplanet systems has been a focus of the astrophyscial community for decades. The primary science goal of such a mission is the direct imaging of Earth analogs, perform spectroscopy of exoplanet atmospheres, and to search for possibly habitable exoplanets. Detectors that are capable for direct exoplanet imaging would detect single photons, high radiation hardness, low power draw, and high dynamic range. The main requirements are: (i) 10^{-10} contrast; (ii) the use of a coronagraph or starshade; (iii) optical and near-IR detection capabilities; (iv) a $R > 70$ IFU able to measure the spectrum of a 30 mag exoplanet; and (v) a 1" radius field of view [41].

2.2 Outline of the SAT Project

To develop QIS technology, the work under the SAT project will include the characterization of three single photon-sensing and photon-number resolving QIS devices with the same detector architecture as the QIS device in the QISPF, but with a revised doping recipe. After extensive laboratory characterization, the QIS technology will reach a technology readiness level (TRL) of 4 representing that the QIS has been validated in a laboratory. An irradiation testing program will simulate damage from high-energy radiation in space found at an orbit around L2, followed by, a telescope demonstration of a non-irradiated QIS. This will advance QIS to TRL 5 from validation in a simulated or realspace environment. In the final part of the project, RIT and Dartmouth will design a QIS image sensor for astrophysics applications.

At RIT, I have been chosen to manage the SAT project. The project has a team of investigators with extensive expertise in astrophysical technology, exoplanet characterization, and the fabrication of CMOS imagers. The team also a team of graduate and undergraduate students. In the months since the start of the project, we have had one Dartmouth graduate student, four RIT graduate students, and five RIT undergraduate students actively participate in the project.

2.3 The progress of the SAT project

The results and investigations presented in this thesis is preliminary work for the larger NASA funded project. From my results, the SAT project team generated requirements for a new electronics design. Much of the high level data acquisition and reduction software has been developed thanks to the experience gained with the QISPF before the project. The current design process has been to determine the software requirements to create low level drivers and identify the modifications required for high level procedures. We also have determined the NASA mission parameters for the radiation testing program that occurs at a later date.

We have held three requirement reviews for the fabrication of new electronics pertaining to the QIS packaging onto a Printed Circuit Board (PCB), the Cold Electronics Board (CEB) that operates the QIS inside our dewar, and the FPGA programming to control the electronics. Following this work, we have created multiple preliminary designs and held three preliminary design reviews.

In the SAT project, we are currently creating the final designs for the detector PCB, CEB, and PCB mechanical mounts. The CfD's pre-existing detector housing for optical testing constrain the physical dimensions of the PCB. SPICE simulations of cable parasitics and thermal contraction calculations demonstrate that the detector PCB satisfies the generated requirements.

2.4 Spatial Resolution and Exoplanet Observations

To prepare for the SAT project, during this thesis I evaluated how the QIS device would be used to make astrophysical observations in LUVOIR and HabEx. When an image sensor observes a point source as found in numerous astrophysical observations, the point source appears as a interference diffraction pattern, referred to as fringes. The fringe pattern is characteristic to the imaging system's aperture and the wavelength of observed light. The Rayleigh Criterion (equation 2.4.1) often evaluates the angular resolution required to distinguish two-point source objects for all imaging systems.

$$\theta = 1.22\frac{\lambda}{D} \tag{2.4.1}$$

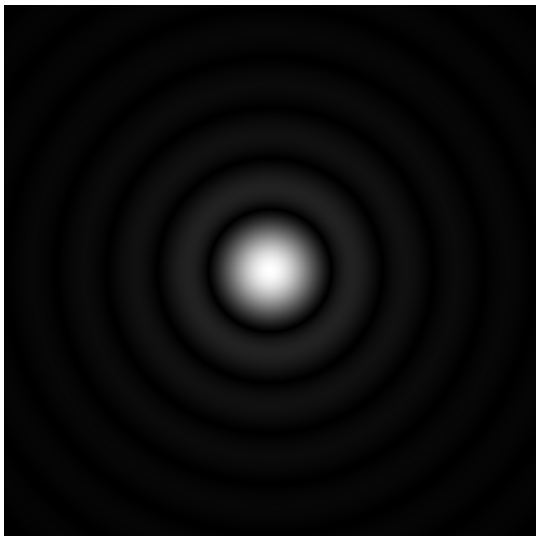

Figure 2.1: simulation of light intensity for an observed point source at the focal plane due to diffraction from airy disk computed by IDL procedure

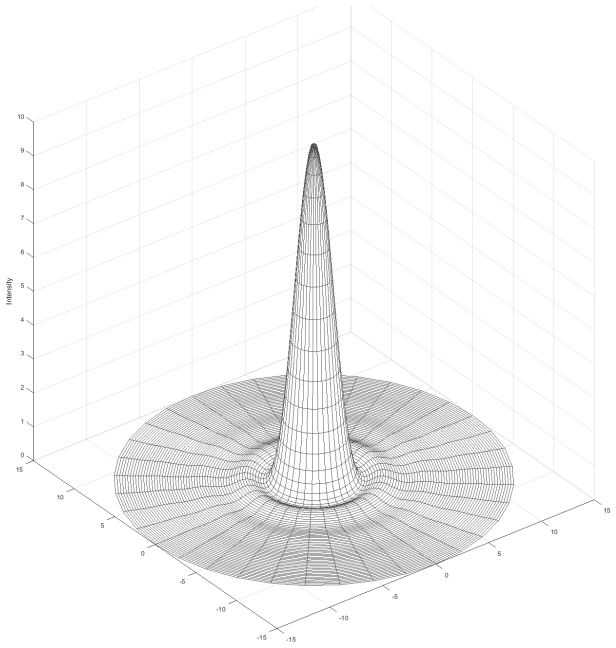

Figure 2.2: point spread function surface plot generated in MATLAB

The diffraction pattern, referred to as an Airy disk (figure 2.1), impacts the maximum resolution for a single point source. This can be mathematically computed using the Airy Function, named after British astronomer George Biddel Airy (1838). The imaged pattern for a single point source is referred to as a point spread function (PSF). The intensity of light from the point spread function can be modeled in a surface plot (figure 2.2).

Nyquist sampling is the typical resolution of a detector array, such as HDI, used for astrophysical imaging. The Nyquist criterion determines the minimum sampling density needed to capture all information preventing aliasing artifacts [42]. For imaging, the Nyquist criterion dictates that the full-width half-max of the PSF central maximum spans the spatial size of two pixels at the focal plane [43]. Using an IDL procedure that simulates the light intensity of a PSF as a function of radius, the central maximum contains 84% of the total intensity of incident light. Considering that the central maximum in figure 2.1 is centered on a pixel, 48% of the total intensity of light is measured by the central pixel. Therefore, the highest signal measured by a pixel when Nyquist sampling should be 48% of the total intensity.

The expected objects observed for LUVOIR and HabEx span a broad range of apparent magnitudes ($m = 12$ to $m = 30$). The QISPF pixel has a size of 1.1 micron and a full-well depth of 200 e^-. Considering that at 48% of the incident light is measured by this pixel, the incident flux measured by a pixel attached to a telescope can be evaluated [44]:

$$F = F_0 \cdot 10^{\frac{m_O - m}{2.5}} \tag{2.4.2}$$

where F_0 is the V-band flux of Vega [photons/s/cm^2/Å], m_0 is the measured apparent V-band magnitude of Vega, and m is the magnitude of the observed object.

From equation 2.4.2 and my knowledge of astrophysics, I derived the following equations to determine the time it would take for a QIS pixel to saturate for the expected observations made with LUVOIR. The observed flux for a telescope can be evaluated as:

$$F_{\text{obs}} = F \cdot A \cdot B \tag{2.4.3}$$

where F_{obs} is the observed flux, A is the area of the telescope (8 m LUVIOR) and B is the bandwidth of the optical filter (V-band). The flux measured by the entire detector array assuming that the array is not vignetting is with a telescope efficiency:

$$F_{\text{D}} = F_{\text{obs}} \cdot QE \cdot \eta_{\text{t}} \cdot N^{T_{\text{m}}} \tag{2.4.4}$$

where F_{D} is the flux at the detector array, QE is the quantum efficiency of the QIS (0.85), η_{t} is the efficiency of the telescope, N is the number of mirrors in the telescope, and T_{m} is the transmittance per mirror. If the object is significantly resolved, then the pixel subtends a solid angle of the observed object:

$$F_{\text{pix}} = F_{\text{D}} \cdot \frac{\alpha_{\text{pix}}}{\alpha_{\text{obj}}} \tag{2.4.5}$$

where F_{pix} is the flux at the pixel, α is the angle subtended on the sky by the pixel (pix) and the observed object (obj). If the object is not resolved and the detector array is Nyquist sampling the point source:

$$F_{pixel} = 0.48 \cdot F_{\text{D}} \tag{2.4.6}$$

$$t = \frac{FW}{F_{\text{pix}}} \tag{2.4.7}$$

where FW is the full well depth of a pixel and t is the time to saturate a pixel. For the QIS, the full well has been simulated at Dartmouth to be 200 e^-. The time to saturate a QISPF pixel, assuming no non-linearities, (table 2.1) can be evaluated from combining equation 2.4.2 and my derived equations, 2.4.3, 2.4.4, 2.4.5, 2.4.6, and 2.4.7.

Table 2.1: QIS pixel saturation time for Nyquist sampling

Apparent Magnitude	Flux at Central Pixel	Central Pixel Saturation Time
12	10,715,572 photons/s	18.7 µs
13	4,265,946 photons/s	46.9 µs
14	1,698,304 photons/s	117.7 µs
18	42,659 photons/s	4.7 ms
24	170 photons/s	1.1 s
30	0.67 photons/s	4.9 min

Chapter 3

Characterization Metrics

3.1 Dark Current

Dark current is the generation of signal that is independent of the light in photo-sensitive materials. Dark current is evaluated as the rate of signal accrued over an integration time under no illumination. For low-light digital imaging, dark current limits detector sensitivity as the dark current rate is comparable in magnitude to the integrated signal. A standard method to mitigate dark current contribution in an image is to subtract a dark frame. A dark frame is an exposure devoid of any incident light. This will remove any fixed-pattern noise from the image, however, this will increase the effective noise generated from dark current by a factor of $\sqrt{2}$. Dark current generation can be categorized into the following contributions:

1. Generation from thermal excitation in bulk material
2. Generation from imperfections in manufacturing
3. Generation from the oxide interface
4. Generation from Tunneling
5. Generation from diffusion current

Dark current in image sensors can vary significantly from pixel to pixel depending on local defects and statistical process variations, leading to some pixels with very high dark current.

The PPD has very low average dark current with state-of-the-art values below 15 e-/s at 60C for a 1.4 um pixel [45].

3.1.1 Generation from Thermal Excitation in Bulk Material

Thermal excitation is the main cause for dark current in bulk materials. Thermal vibrations from phonons in a semiconductor lattice can excite valance electrons to overcome the band gap energy of the semiconductor. As a result, the valance electron enters the conduction band where it can be captured by a pixel's potential well and measured as signal. The Maxwell-Boltzmann distribution describes the distribution of thermal vibrations which dictates the excitation energy. Thus, the warmer the device, the higher the dark current (equation 3.1.1 and 3.1.2).

Thermal generation/recombination events occur commonly in photo-sensitive materials. Defects, called traps, in the bulk material restrict the movement of electron-hole pairs. Trap assisted generation-recombination events in silicon are typically the dominant contribution to dark current compared to other generation-recombination mechanisms [46].

$$D = C \cdot A \cdot I_d \cdot T^{1.5} \cdot e^{\frac{E_g}{2kT}} \tag{3.1.1}$$

where D is the dark current ($e^-/pixel/s$), C is a numerical pre-factor that depends on the photosensitive device, A is the pixel area cm^2, I_d is the dark current at 300 K (nA/cm^2), E_g is the bandgap at temperature T, and T is the temperature in Kelvin. The bandgap of silicon varies with temperature according to [47]:

$$E_{\mathrm{g}} = 1.1557 - \frac{(7.021 \cdot 10^4) \cdot T^2}{1108 + T} \tag{3.1.2}$$

3.1.2 Generation from Imperfections in Manufacturing

A pixel randomly generates signal from imperfections in the material such as impurities, mismatch of atomic lattices, or dislocations. Imperfections in the manufacturing process cause a physical location in the array to have a different dark current generation rate when compared

to the rest of the CMOS array. Hot pixels are pixels that exhibit significantly heightened dark current from these generation sites [48]. Since this effect arises mostly from defects in the crystal lattice, hot pixels will typically never move in location nor disappear. Therefore, hot pixels can easily be removed from the data once found [49]. Hot pixels may also be generated after manufacture from damage, mechanical stress, or radiation damage that alter the lattice of a pixel. This allows the number of hot pixels to grow over a detector's lifetime.

3.1.3 Generation from the Oxide Interface

At the interface of Si and SiO_2, the mismatch of the two lattices generates considerable dark current caused by the large number of surface states formed during manufacture [50]. Thermal treatment during and after the growth of the oxide reduces the number of these states. More specifically, hydrogen can diffuse into the interface and fill the mismatched bonds [51]. However, it is impossible to remove all such centers of dark current generation. Typically, dark current generation from the oxide interface can have considerably more generation centers than within the bulk material.

3.1.4 Generation from Tunneling

Charge carriers in the valence band penetrate, or tunnel, through a thin band-gap into the conduction band. This is a common phenomenon found in heavily doped p-n junctions where the electric field is great enough to allow carriers to tunnel through the p-substrate to the n+ depletion region of a photodiode [52].

Once entering the depletion region, the carrier contributes to the measured dark current of the pixel. It is possible to mitigate this issue at the Si-SiO_2 interface by adding a thin p-doped layer in-between that captures free carriers that would normally go into the depletion region.

3.1.5 Generation from Diffusion Current

Diffusion current is movement of charge carriers due to a gradient in the electric potential. The electric potential gradient is caused by differences in the doping concentration (equation

3.1.3). During fabrication, a region of a p-n junction may become slightly more or less doped than the surrounding area causing a gradient in the concentration level [53]. Charge carriers tend to move from a higher concentration to a lower concentration generating a current in the material. Careful fabrication and reducing detector temperature lowers thermal agitation of carriers and mitigates diffusion current. Dark current due to diffusion current of electronics can be evaluated as:

$$J_{\text{diff}} = \frac{qD_{\text{n}}n_{\text{p0}}}{L_{\text{n}}} = q\sqrt{\frac{D_{\text{n}}}{\tau_{\text{n}}}} \cdot \frac{n_{\text{i}}^2}{N_{\text{A}}} \tag{3.1.3}$$

where J_{diff} is the diffusion current due to electrons, n_{p0} is the electron concentration at the boundary condition, D_{n} is the electron diffusion coefficient, L_{n} is the diffusion length, τ_{n} is the carrier lifetime, and n_{i} is the intrinsic concentration which is a temperature dependent quantity.

3.1.6 Dark current and the QIS

In an ideal detector diode, the most important contributors to dark current include charge diffusion, thermal generation-recombination of charges within the bulk of the semiconductor, and small leakage currents generated by surface states. Most of the dark current will be dominated by thermal generation-recombination that decreases with decreasing temperature, and surface leakage currents that have similar temperature dependence. For the QIS, the background light level for optical wavelengths inside the dewar is expected to be low enough to enable dark current measurements at a level of 0.0001 e^-/s/pixel. From the results of this thesis, I computed the expected dark current rate of the QIS will be 0.0003 e^-/s/pixel at 150 K.

3.2 Temporal Noise

Temporal Noise is the variation in a pixel's response under constant or no illumination. Temporal noise is evaluated by computing the standard deviation of a pixel's response over multiple

measurements or frames. The standard deviation of all pixels computes the average noise for the detector. In general, temporal noise consists of multiple noise contributions [54]:

1. Shot Noise
2. Johnson Noise
3. 1/f Noise
4. kTC Noise
5. ADC quantization
6. EMI, Timing Jitter, and other electronics

3.2.1 Shot Noise

Shot noise is noise associated with the random generation of charge carriers. Ideally, the generation of charge carriers is only due to the random arrival time of photons characterized by Poisson statistics (equation 3.2.4). The uncertainty, or shot noise, can therefore be evaluated as follows:

$$\sigma_{\mathrm{n}} = \sqrt{S} \tag{3.2.4}$$

where S is the signal and σ_{n} is the shot noise. From section 3.1, we can recall that incident light, S_{P}, is not the only contribution to the measured signal of a pixel. The random generation of electron-hole pairs due to dark current, S_{DC}, also contributes to shot noise (equation 3.2.5). As dark current also follows Poisson statistics, the above equation can be rewritten where shot noise is represented as:

$$\sigma_n = \sqrt{S_{\mathrm{P}} + S_{\mathrm{DC}}} \tag{3.2.5}$$

3.2.2 Johnson Noise

Johnson noise, also referred to as thermal noise, is noise associated with the thermal agitation of charge carriers in a resistive medium (equation 3.2.6). Johnson noise is independent from the current flow and is characterized as a random (white) noise [55]. For imaging sensors, there are three typical locations where Johnson noise generates a voltage uncertainty: i) Thermal noise generated by the channel resistance of a FET; ii) the output impedance of the SF; iii) noise from discrete resistors. Johnson noise can be characterized in volts as:

$$\sigma_{\mathrm{T}} = \sqrt{4kTBR} \tag{3.2.6}$$

where σ_{T} is the thermal noise, k is the Boltzmann constant, T is the temperature of the resistive medium, B is the bandwidth of the system, and R is the total resistance of the medium. Equation 3.2.7 demonstrates how Johnson noise can be represented in electrons when utilizing the charge to voltage factor and the output amplifier gain.

$$\sigma_{\mathrm{T}} = \frac{\sqrt{4kTBR}}{(\frac{\Delta V}{\Delta N})A_v} \tag{3.2.7}$$

where $(\frac{\Delta V}{\Delta N})$ is the sensitivity (V/e^-) and A_V is the amplifier gain.

3.2.3 1/f Noise

1/f noise, also referred to as flicker noise or random telegraph signal, is a type of noise where the power density decreases with increasing frequency. More specifically, the noise power (V^2/Hz) decreases by a factor of 10 for each decade increase in frequency. The exact origin of 1/f noise in imaging sensors is an ongoing area of research but it is clear that 1/f noise is common as it is found in many natural systems in our universe. Examples of 1/f noise include: coupled processes in climate change, sound acoustics, gravitational wave astronomy, and electronic devices. For imaging sensors, it is accepted that 1/f noise generates from traps in the silicon-oxide interface of FETs where the effective time constant for the release of trapped electronics is randomly distributed [56]. The superposition of all random release events generates a 1/f

noise spectrum (equation 3.2.8). 1/f noise is pronounced in FETs with small channels where the 1/f voltage noise can be evaluated as:

$$\overline{V_{1/f}^2} = \frac{K_f}{wLC_{\text{ox}}}\frac{\Delta f}{f} \tag{3.2.8}$$

where K_f is a fabrication process-dependent constant and is typically around $3x10^{-24}\ V^2F$, Δf is the bandwidth of the FET, C_{ox} is the capacitance of the FET, w is the width of the FET, and L is the length of the FET.

3.2.4 kTC Noise

kTC noise, or reset noise, is thermal noise associated with a reset switch sampled over a capacitor. In a capacitor, thermal agitations redistribute charge with an uncertainty in voltage. The act of resetting a capacitor freezes the redistribution into a random fluctuation of charge. In image sensors, the FD capacitance connected to the gate capacitor of the reset FET is the main generation of kTC noise (equation 3.2.9). CDS is performed to remove reset noise from the final measurement. kTC reset noise can be characterized by the following:

$$\sigma_{\text{res}} = \sqrt{\frac{kT}{C_{\text{pd}}}} \tag{3.2.9}$$

where σ_{res} is the reset noise, k is the Boltzmann constant, T is the temperature in Kelvin, and C_{pd} is the diffusion capacitance or floating node capacitance. Equation 3.2.10 demonstrates how kTC noise can be represented in electrons by considering the self-capacitance of a conductor relationship.

$$\sigma_{\text{res}} = \sqrt{\frac{kTC_{\text{pd}}}{\text{e}^-}} \tag{3.2.10}$$

3.2.5 ADC Quantizaton

Quantization noise from the ADC results from mapping a range of analog voltages into discrete digital values. Every ADC is rated for a range of input analog voltage. The input signal can

by any of the infinite voltages within such a range, however, the ADC must break this range up into discrete sections related to the ADC bit resolution. As such, a subset of the voltage range will be assigned to the same ADC output value.

To mitigate quantization error, one chooses an ADC that will add a negligible amount of noise to the signal noise when added in quadrature. The standard deviation of ADC quantization is related to the least significant bit (LSB) in equation 3.2.11:

$$\sigma_{\text{ADC}} = \frac{1}{\sqrt{12}} LSB \approx 0.29 LSB \tag{3.2.11}$$

Considering an analog signal with amplitude A and a root-mean-square voltage noise of σ, an optimal ADC resolution n is chosen that satisfies equation 3.2.12.

$$(\frac{2^n \sigma}{A}) \approx \sqrt{(\frac{2^n \sigma}{A})^2 + (0.29)^2} \tag{3.2.12}$$

It is tempting to choose an ADC with the highest possible resolution. However, if equation 3.2.12 is satisfied, a higher resolution ADC will not provide more information. In fact, higher resolution ADCs take a longer time to sample than their lower resolution counterparts, decreasing the maximum possible sampling rate.

3.2.6 Temporal Noise and the QIS

For QIS, it is believed that noise from the in-pixel source-follower (SF) transistor dominates the read noise. SF noise is composed of several different types of noise, mainly 1/f noise or flicker noise, random telegraph noise (RTN), and thermal noise (or Johnson–Nyquist noise). The QIS is designed to be sensitive to single photoelectrons and so single-trap or multi-traps-induced RTN can be observed. However, there exists a lower-level of background noise in addition to the RTN [32]. The single photon sensing ability of the QIS allows for the investigation of 1/f noise models.

3.3 Charge to Voltage Factor

The charge to voltage factor (CVF) is the relationship between the voltage signal, V_S response of a pixel to the number of generated electrons (equation 3.3.13).

$$CVF\,[\mu V/e^-] = \frac{V_S}{\mu_e} \tag{3.3.13}$$

The CVF can be measured in a variety of different but similar methods. On method is to use the photo response curve. The response curve gives the relation between output voltage and the incident number of photons. Having knowledge about the quantum efficiency converts the number of photons into the number of generated electrons which evaluates the relationship between output voltage and the electronic charge.

An alternative method to determine CVF is the photon transfer, or mean-variance, curve [57]. The photon transfer curve compares the photon shot noise to the square root of the average voltage signal level. Statistically, the shot noise from photons is proportional to the square root of the voltage signal level (equation 3.3.13) where CVF is the slope of the curve:

$$\sigma_n = \sqrt{q \cdot V_S} \tag{3.3.14}$$

where σ_n is the photon shot noise and V_S is the output signal and q is the fundamental electron charge. Hence, CVF can be determined from the slope of variance σ_n^2 as a function of mean signal.

A final method relies on the photon-number resolution of a detector. This method, which is used in this thesis, is the photon counting histogram method [58]. A photon-number resolving detector can inherently resolve the individual number of electrons measured in a pixel. This measurement will be digitized and assigned a digital number by the readout electronics. This allows for a direct measurement of the ADC conversion gain [ADU/e^-], where ADU is the digital output of the ADC for an input analog signal. If the reset voltage is allowed to vary and the output digital number is measured, an electronics gain [µV/ADU] can be measured. These two values can be combined to compute the CVF.

3.3.1 CVF and the QIS

Single photon sensing is difficult because the electron charge is very small and the resultant voltage is typically less than the noise level of the read circuit. Non-QIS photon counting devices, such as single-photon avalanche diode (SPAD) and electron-multiplying CCD (EM-CCD) [59] detectors, use avalanche multiplication to achieve enough charge gain for photon sensing. However, the avalanche process contains numerous downsides including high sensitivity to silicon defects from high electric fields, high dark count rates, sensitivity to bias and clocking voltages, and lower resolution than CMOS image sensors [60]. The primary goal of QIS development was to not use avalanche multiplication but to increase the charge to voltage factor so that a single electron would generate a signal that was much higher than the read noise of the device. Typical CMOS sensors have a CVF of 10 - 50 $\mu V/e^-$ [14], where published values of the QIS measure a CVF $>$350 $\mu V/e^-$.

3.4 Quantum Efficiency

As described in section 1.1, a photon excites an electron into the conduction band of a semiconductor where electronics measure and digitize the electron signal. The quantum efficiency (QE) of an image sensor is the measurement of how good that sensor can detect light. QE (equation 3.4.15) is the ratio of the number of photo-generated electrons measured at the output of the image sensor to the absolute number of photons that hit the detector over the integration time.

$$QE(\lambda) = \frac{N_{e^-}}{N_{pho}} \tag{3.4.15}$$

As photons pass through a semiconductor material, the rate of photon absorption is proportional to the intensity of photons for a given wavelength (equation 3.4.16). The number of photons that reach a certain depth in the semiconductor depends on the wavelength of the photons (equation 3.4.17). The intensity of photons of a single wavelength can be evaluated as:

$$F(x) = F(x_0)e^{-\alpha(x-x_0)} \tag{3.4.16}$$

where $F(x)$ is the intensity at a depth below the surface, $F(x_0)$ is the unattenuated intensity at the surface x_0, and α is the absorption coefficient. The absorption coefficient characterizes a materials ability to absorb the photon at a wavelength. This is expressed as:

$$\alpha = \frac{4\pi k}{\lambda} \tag{3.4.17}$$

where k is the material dependent extinction coefficient.

In the field of CMOS image sensors, one typically measures QE across the full wavelength range that a detector responds to light. QE is expressed as a percent or a value from zero to one. Readout electronics also have an efficiency that decreases the calculated QE of an image sensors. Thus, it is difficult for an image sensor to have a QE equal to the theoretical QE of the photosensitive material. Nearly every CMOS image sensor is fabricated using a silicon material where quantum efficiency of a pixel is governed by the design of the photodiode and the quality of the manufacture process.

The ideal detector exhibits a QE of 100 percent where every incident photon is measured by the detector. However, there are many limitations that prevent the production of an ideal detector such as photons reflecting off the materials surface or photon interference, seen in results figure 4.27), due to different layering in the semiconductor. Additional limitations arise from the design of the photosensitive area. The depletion region cannot consist of the entire area of the pixel. Thus, photons can generate electron-hole pairs outside of the depletion region that may not random walk into the depletion region. Additionally, the electric potential of the oxide layer near the surface can trap electron-hole pairs. This effect is apparent from short wavelength photons that have a small average depth of absorption. If the depletion region is too shallow, photons of longer wavelength may absorb below the photosensitive area or pass through through the silicon.

Chapter 4

Initial Setup, Testing, and Results

The following section describes the basic measurement procedures for all characterization metrics of the CMOS image sensor presented in this work. Each characterization section outlines the goal of the measurement, the experimental procedure, and the data reduction and analysis pipeline. The final section for each characterization metric will present the measured results and the analytical interpretation of the results.

Initial testing of the QISPF focused on understanding the operation of the QIS chip and the QISPF camera system in-order to develop an entire automatic test suite, create `IDL/C/C++` drivers, and identify differences of the QIS compared to previous image sensors tested at the CfD. Following this, the automated test suite performed experiments to measure dark current, total noise, quantum efficiency, ADC conversion gain, electronic gain, and charge to voltage factor. With the automated test suite, a user enters a single command line into IDL and walks away while a multi-day test suite occurs on its own.

4.1 The Test Suite

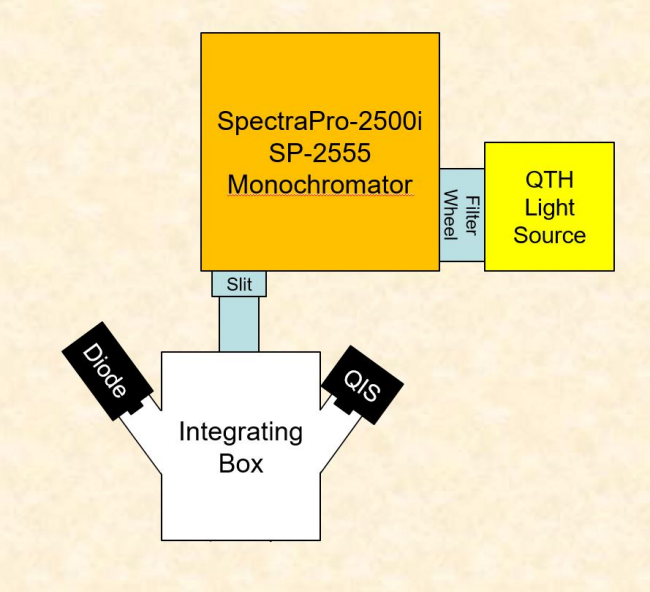

Figure 4.1: QISPF test suite diagram

All measurements presented are performed using the same system setup (Figure 4.1) that an IDL procedure modifies to suit the needs of any experiment. The system includes the following components:

1. the QISPF camera system
2. calibrated monitoring Si Diode
3. integration box
4. monochromator
5. monochromator slit
6. optical filter wheel
7. adjustable light source

Light is generated by an adjustable 3200 K Quartz Tungsten Halogen (QTH) bulb. The light will pass through a filter wheel with an open position, four filters, or a closed position to block all external photons from the light source. The filter wheel is mounted onto the side input of a Princton Instruments Action SpectraPro-2500I triple-grating spectrometer/-monochromator. This SpectraPro-2500I is fitted with the following gratings: UV-optical (0 nm to 700 nm), optical-NIR (700 nm to 1200 nm), and IR (1200 nm to 6000 nm). The output of the monochromator passes through an adjustable slit. The slit controls the wavelength bandpass and, indirectly, the intensity of light. The slit is typically set to a slit size of 3 mm which corresponds to a bandpass of 10 nm. The output of the monochromator slit enters a hand-made integrating box lined with standard copy paper. An integrating box was made by hand as the integrating spheres at the CfD are coated with materials designed for IR detector testing. The integrating sphere originally used was coated with infra-gold, a great material for diffuse IR reflection, but poor UV-optical reflectance properties at wavelengths shorter than 500 nm.

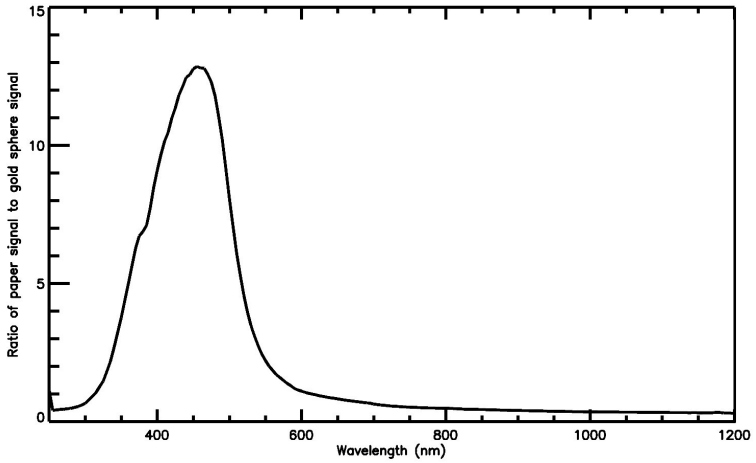

Figure 4.2: ratio of calibrated diode response for infra-gold integrating sphere vs paper integrating box response as a function of wavelength

While the hand-made integrating box does not out perform a professional integrating sphere at wavelengths longer than 500 nm, the integrating box provides an increase of 13x the light intensity over the the infra-gold integrating sphere around 425 nm (figure 4.2). In

the quantum efficiency results discussed later in this thesis, it is clear that the integrating box is preferred over the infra-gold integrating sphere because the intensity of the QTH light source degrades significantly for sub-600 nm wavelengths. This presented a major challenge to measure the quantum efficiency at short wavelengths.

4.2 The IDL Drivers and Data Pipeline

A considerable amount of time during this thesis was spent designing and creating the camera drivers that would enable the Opal Kelly XEM7310 to communicate and be supported by IDL. This was fundamental for the CfD standard data acquisition and reduction pipeline to operate the QISPF.

The QISPF and the test suite are controlled by multiple IDL procedures. The power of the adjustable light source is the only component of the test suite that cannot be changed from IDL. Rather, the monochromator slit controls light intensity where increasing the slit width increases the wavelength bandpass allowing more light to enter the integrating box.

While a user enters a single command line on the acquisition computer connected to the QISPF, a second reduction computer on the network will perform the data reduction and analysis automatically. After a user has entered a single command line, the automatic procedure for all test suites contains the following steps:

1. read in parameters for a characterization experiment
2. determine the domain computer and connected detector
3. create all folders for raw data
4. prepare monochromator and filters for initial dark exposure
5. initialize dewar electronics
6. configure Opal Kelly FPGA
7. initialize the QISPF DACs

8. perform initial dark exposure
9. prepare monochromotor and filters for experiment
10. perform data acquisition
11. deinterlace raw data
12. save data to a fits file
13. copy data to reduction computer
14. send completed acquisition email
15. start data reduction on reduction computer
16. save reduced data
17. perform analysis on reduced data
18. save figures and analyzed data
19. send completed data reduction email

The automated IDL data reduction and analysis utilizes a standard Gaussian fit to evaluate the mean value and width of all histograms. The procedure will also plot a cumulative curve that evaluates the cumulative number of pixels from the entire detector array. This is important to note as not all histograms represent a perfect Gaussian distribution such as in the temporal noise results.

4.3 Dark Current

Dark current is one of the most important characteristics of any image sensor and is one of the easiest to measure. Dark current can be evaluated as the rate of signal that will accrue over a time when devoid of light. The experimental procedure to measure dark current can be summarized as taking images in an area devoid of light while making variations in temperature

and integration time. Due to limitations of the design of the QISPF camera system, variations in temperature cannot be explored until a cryogenically (down to 150 K) compatible packaging is created.

4.3.1 Measurement Procedure

The image sensor measures the signal of a pixel when in a dark environment at various integration times. A linear fit to the output signal over integration time evaluates the dark current in digital units per second [ADU/s]. This measurement can be represented in [µV/s] as well as [e^-/s] when combined with the results from the charge to voltage conversion factor experiment.

The dark current test suite starts by initializing the electronics of both the QISPF and the test suite. First, filters are closed to prevent any excess light from entering the integrating box and hitting the detector array. Next, the QISPF is initialized by establishing a link to the XEM 7310, configuring the FPGA with a configuration bit file, and setting all DAC controlled voltages. The FPGA configuration file contains the information that controls whether the QISPF performs sequential or simultaneous pulsing of the photodiode transfer gates, TX1 and TX2. It was eventually determined that the typical dark current experiment of the QISPF should perform TX1 and TX2 simultaneously due to leakage current over TX connecting the PPD to the FD as described in a later section.

The QISPF will start the experimental procedure by capturing 100 frames of initial dark current data at the shortest integration of 50 µs. The initial dark measurement is a standard procedure to remove any residual signal from a previous experiment or from before the filter wheel was closed. After this, the QIS now performs dark current exposures at multiple integration times. The range of integration times for the simultaneous transfer of charge from both TX1 and TX2 is 50 µs to 25 ms. With a more recent configuration from Gigajot, measurements can be performed up to an integration of 2 minutes. The integration time resolution in the range of 50 µs and 25 ms is 50 µs. The integration time resolution in the range of 25 ms to 2 minutes is 25 ms.

The dark current test suite only uses a subsection of all possible integration times. The QISPF captures 10,000 frames for each integration time. The dark current is evaluated by two methods. The first method evaluates a dark current for each pixel. The second method evaluates the effective dark current of the entire array.

The dark current for a pixel is evaluated as the average of 10,000 CDS measurements at an integration time. For normal image sensors, the average signal would be subtracted by a short integration time to remove any fixed-pattern noise which would cause particular pixels to be measure a heightened or lowered signal than the rest of the detector array. For the QIS, the reset samples are performed immediately before the transfer of charge and the signal samples. Not only is the reset noise removed but, any fixed-pattern noise from dark current as well.

The dark current for the array is evaluated from a linear fit the average signal across the range of integration time. In this method, all pixels are assumed to be identical and the entire data cube of 10,000 frames is averaged into a single value for a given integration time. A linear fit to the average signal as a function of integration time evaluates the dark current.

4.3.2 Dark Current Results

In figure 4.3, the integrated dark signal is measured for integration times greater than 25 ms. The integrated dark signal responds linearly between 0.5 s to 1.5 s with a linear slope of 0.058 e^-/s. The non-linearity at integration times shorter than 0.5 s contains a considerable dark count rate. This may be due to the settling of charges after reset on the floating diffusion but this will need to be further investigated. A pattern of higher dark signal at specific integration times is also apparent, however, it is currently unknown what causes the pattern seen in the dark signal. During the SAT project, this phenomenon will be investigated across multiple different detectors.

For the above result, TX1 and TX2 occur at the same time were the measured signal is from two pixels. To correct for this, the slope is divided by 2 calculating a dark current of $0.028e^-/s/pixel$. The current configuration at CfD for the XEM7310 do not allow for TX1 and TX2 to occur sequentially for integration times longer that 38 ms.

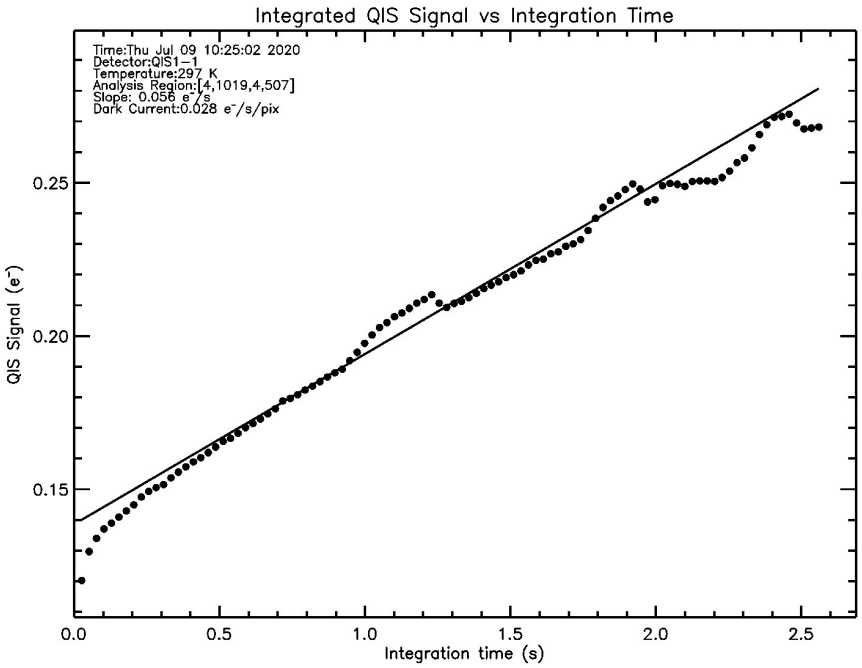

Figure 4.3: integrated dark signal up to 2.5 s

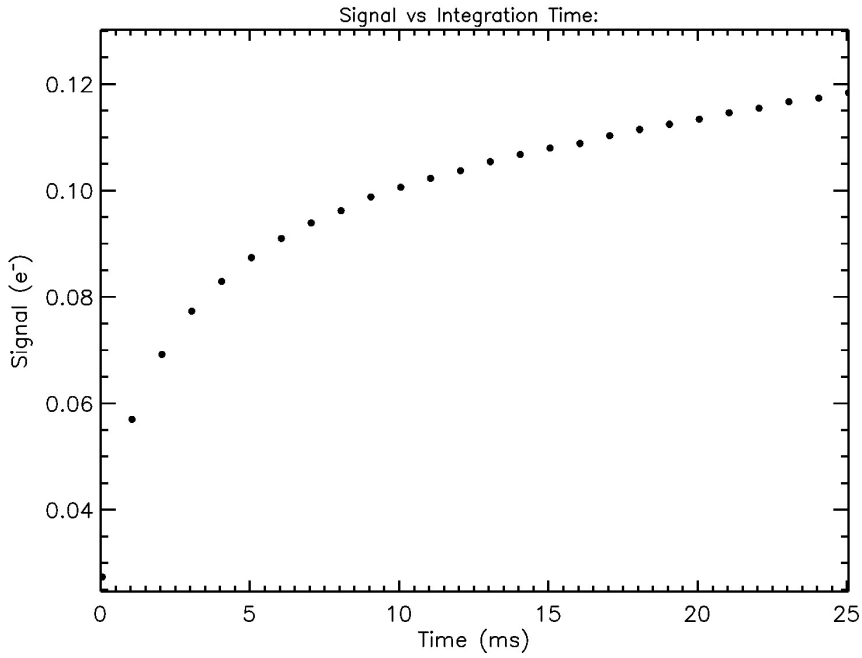

Figure 4.4: integrated dark signal with simultaneous charge transfer

Integrated dark signal can also be measured at much smaller integration that 25 ms. Figure 4.4 demonstrates these measurements when TX1 and TX2 are simultaneous. While integrated

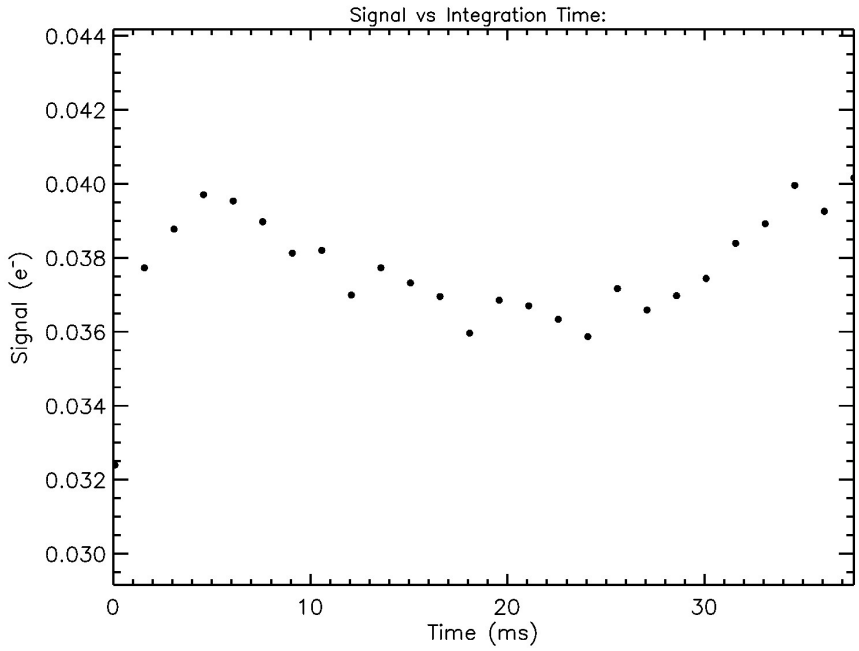

Figure 4.5: integrated dark signal with sequential charge transfer

dark signal between 10 ms - 25 ms appears to be linear, this is not the case shown in figure 4.3. A linear fit to the integrated signal (not shown in the figure) between 10 ms - 25 ms computes a integrated dark signal of approximately 1 e^-/s for two pixels which is significantly larger than the dark current at longer integration times. Figure 4.5 is the same dark signal measurement but TX1 and TX2 occur sequentially. The transfer of charge for TX1 is followed by a set of signal samples for TX1. During this time, TX2 is integrating with charge carriers collecting in the SW. Ideally, the charge carriers stay in the SW, however, charge leaks across TX2 onto the FD. During CDS, the reset level for TX2 is actually the previous signal samples for TX1. Because TX1 is measured first, the sampled change in FD voltage for TX1 comprises of both the transferred signal from TX1 and the leakage current from TX2. When TX2 transfers charge, leakage current has reduced the total collected charge in the SW for TX2 resulting in a smaller change in FD voltage.

The smaller change in FD voltage during TX2 is found in the a bimodal distribution in figure 4.7 compared to figure 4.6. This is also an apparent in figure 4.9 as a fixed pattern where every other row of 1024 pixels has a significant decrease in the evaluated integrated

signal which corresponds to the two-way shared architecture of the FD.

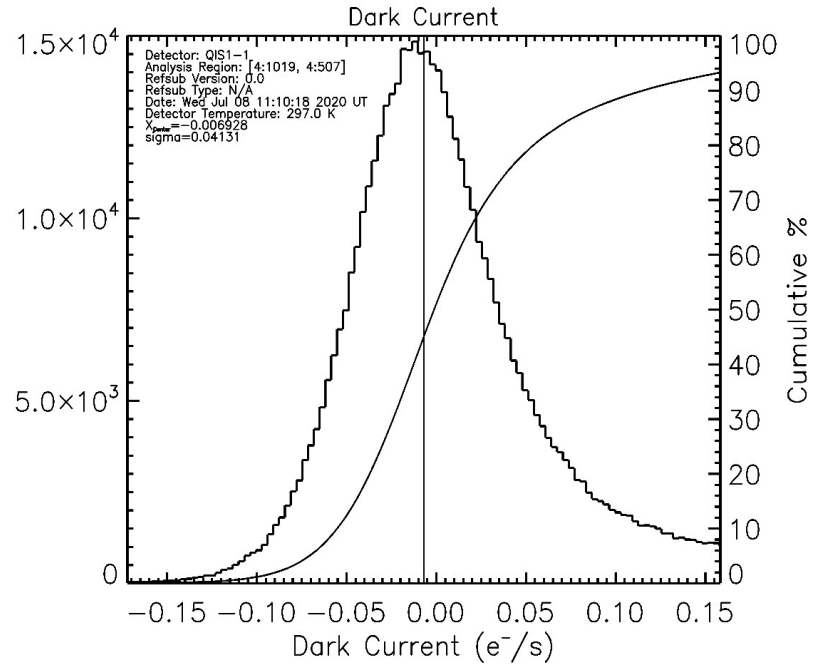

Figure 4.6: histogram of the dark current with simultaneous charge transfer

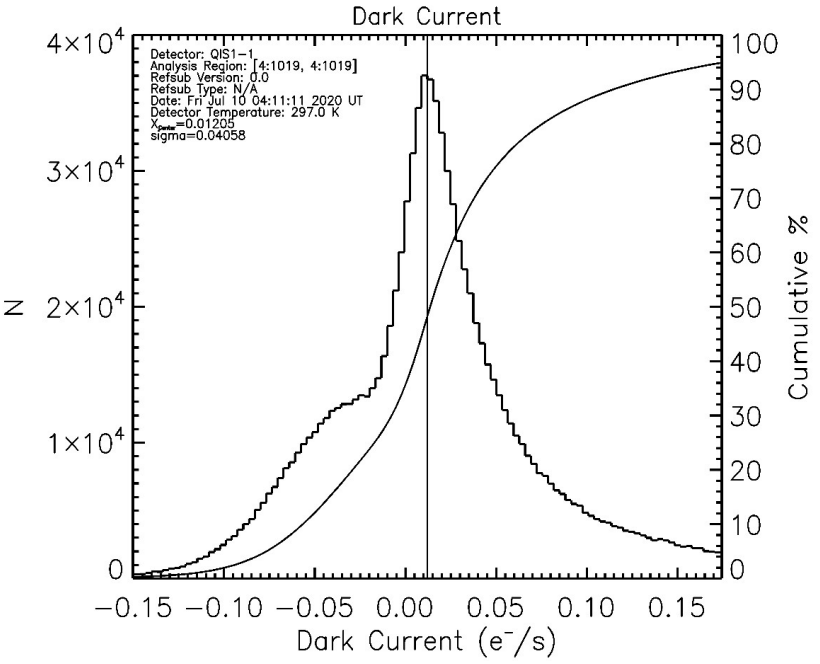

Figure 4.7: histogram of the dark current with simultaneous charge transfer

Figure 4.8: map of the mean dark signal [e^-] with simultaneous charge transfer

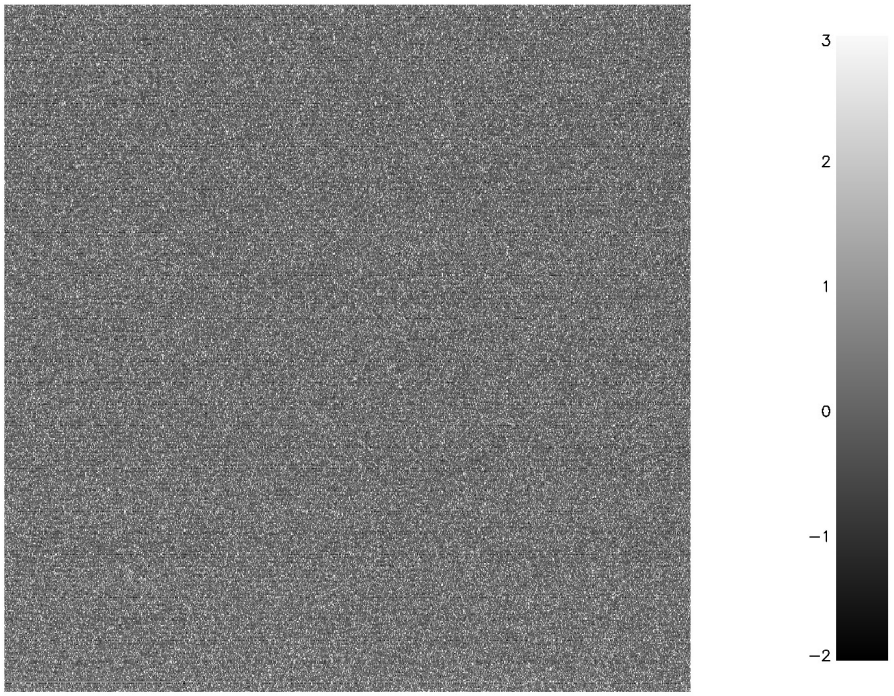

Figure 4.9: map of the mean dark signal [e^-] with sequential charge transfer

4.4 Temporal Noise

Temporal noise, or total noise, can be evaluated as the variation of a pixel's response under a constant or no illumination. To characterize the properties of an image sensor, one chooses to perform measurements under no-illumination to remove any shot noise generated from the random arrival time of photons. The experimental procedure can be summarized as taking multiple images in an area devoid of light and computing the standard deviation of each pixel's response.

4.4.1 Measurement Procedure

The automated total noise data reduction uses the raw data from the dark current experiment. The image sensor measures the signal of a pixel multiple times for different integration times. The total noise of the device is computed as the standard deviation of each pixel's response at a given integration time. As total noise is calculated from the dark current experiment, both results can be combined to evaluate the total noise as a function of the integrated signal.

The total noise test suite starts by initializing the electronics of both the QISPF and the test suite. The IDL procedure closes the filter wheel to create a dark environment. As with dark current, we choose to perform TX1 and TX2 simultaneously due to leakage current.

The QISPF starts the experimental procedure by capturing 100 frames of initial dark current data at the shortest integration of 50 µs followed by the acquisition of raw data. The range of integration times for the simultaneous transfer of charge from both TX1 and TX2 is 50 µs to 2 minutes. The integration time resolution in the range of 50 µs and 25 ms is 50us. The integration time resolution is 25.6 ms for the range of 25 ms to 2 minutes.

Total noise is computed from 10,000 frames from a subsection of all possible integration times. IDL procedures evaluate total noise in two methods. The first method evaluates a total noise for each pixel as the standard deviation of that pixel's measurements for an integration time. The IDL procedure then creates a histogram of all pixels' computed standard deviation. The second method evaluates the shot noise generated from integrated signal by plotting the average total noise as a function of integration time. Further analysis is performed by

combining the dark current and total noise results in a plot of total noise as a function of the integrated signal.

The QISPF performs 2,4,8, or 16 CDS samples to average. The number of samples refers to the number of reset and corresponding signal samples that will be performed. For example, if the FPGA configuration performs 16 CDS samples, a total of 34 samples are performed. The first 17 samples correspond to the reset samples where the first sample is not used in the averaging process. Immediately following the reset samples, 17 additional signal samples are performed where the charge is transferred at the same time as the first signal sample. This also is not used to compute the average signal samples. The process of averaging multiple samples is similar to the process found in Fowler sampling. In Fowler sampling, the reset samples are performed at the beginning of a pixels integration. In the QISPF, the reset samples are actually apart of the signal samples. The division between reset and signal sampling occurs when TX is pulsed high as shown in (figure 1.9).

4.4.2 Temporal Noise Results

At integration times larger than 25 ms the QISPF total noise is greater than 0.5 e^- with a linear increase of 0.07 e^-/s (figure 4.10). Considering that dark current per pixel is measured at 0.028 e^-/s/pix (figure 4.3), the increase in total noise is not solely due to the shot noise generated from dark current. The shot noise should be equivalent to an increase in noise of 0.167 e^-/s. At such a high noise, the QISPF would no longer exhibit photon-number resolving capability.

At integration times less than 25 ms, the QISPF maintains a total noise of less than 0.5 e^- with 16 CDS samples (figure 4.11). The QISPF camera system is designed to operate at small integration times to maintain the photon number resolution capability of the device. The total noise of the QISPF will increase as less samples are performed as seen in figures 4.12, 4.13, 4.14, 4.15, and 4.16. The following histograms for total noise are performed at the shortest possible integration times where the shortest integration time is dependent upon the time it tasks to perform a single sample at a rate of 526 kHz (table 4.1).

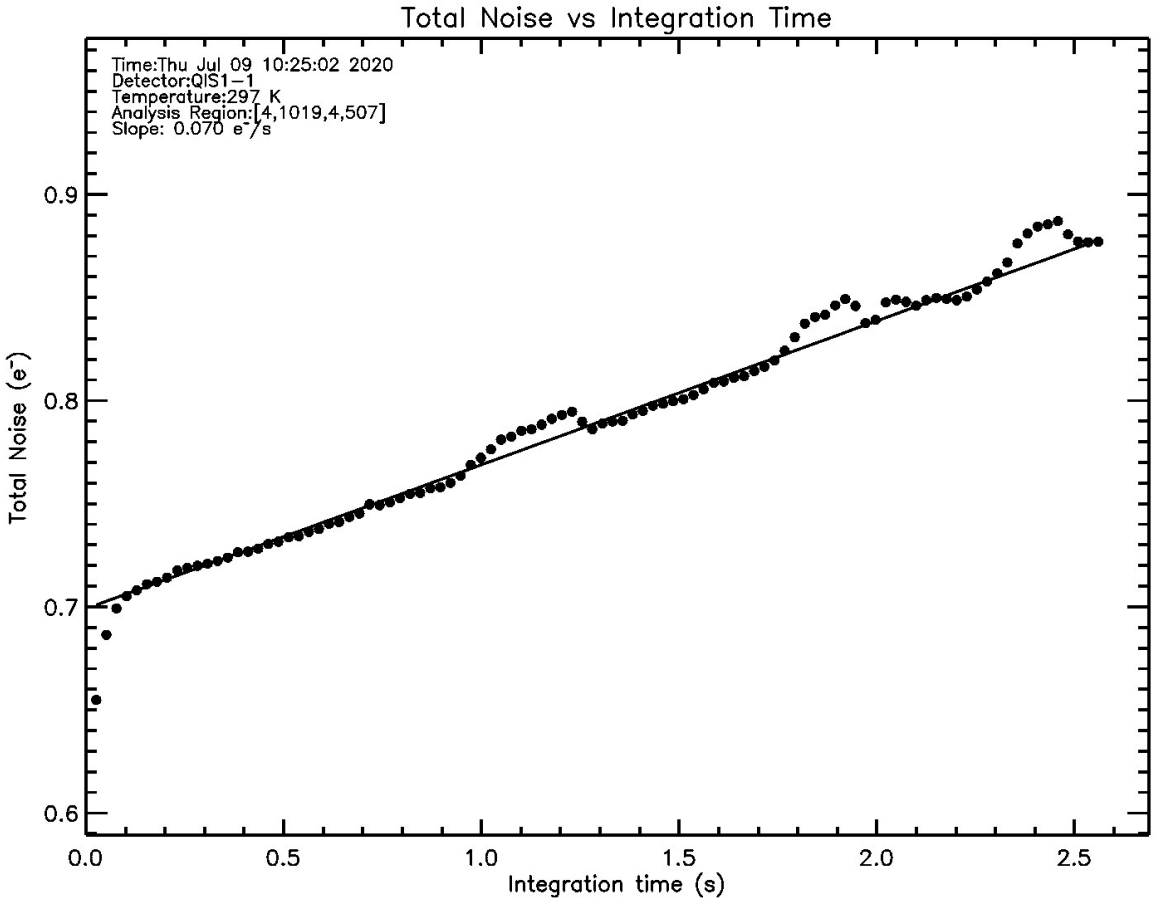

Figure 4.10: total noise with integration time greater than 25 ms with 16 CDS samples

Table 4.1: number of CDS samples effect on total noise and integration time

CDS Samples	TX Mode	Total Noise	Shortest Integration
2	Simultaneous	0.58 e^-	23 µs
4	Simultaneous	0.44 e^-	26 µs
8	Simultaneous	0.35 e^-	34 µs
16	Simultaneous	0.31 e^-	50 µs
2	Sequential	0.58 e^-	21 µs
4	Sequential	0.44 e^-	29 µs
8	Sequential	0.35 e^-	44 µs
16	Sequential	0.31 e^-	74 µs

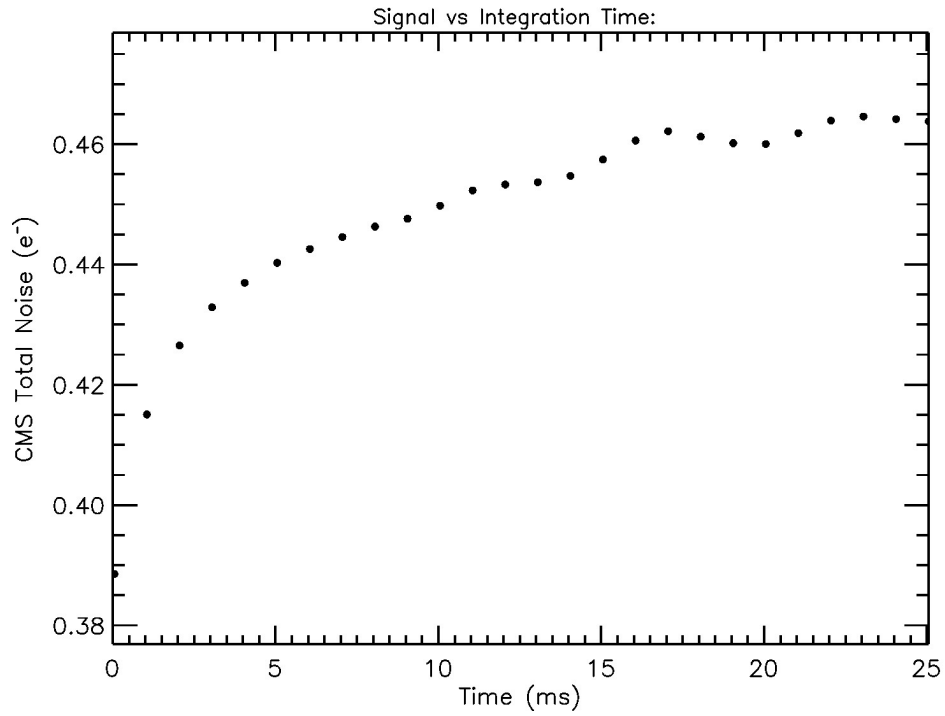

Figure 4.11: total noise for integration less than 25 ms with 16 CDS samples

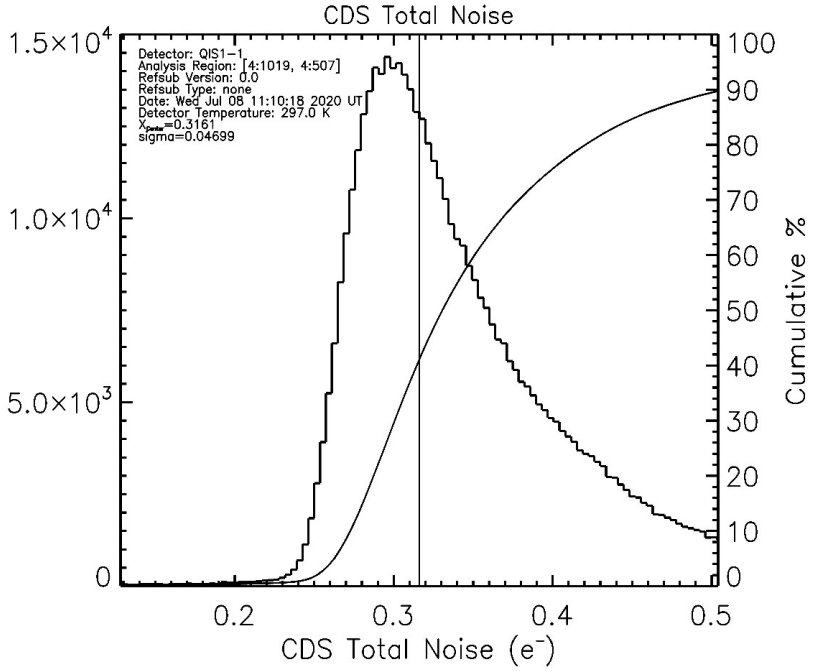

Figure 4.12: histogram of total noise with 16 CDS samples with simultaneous charge transfer

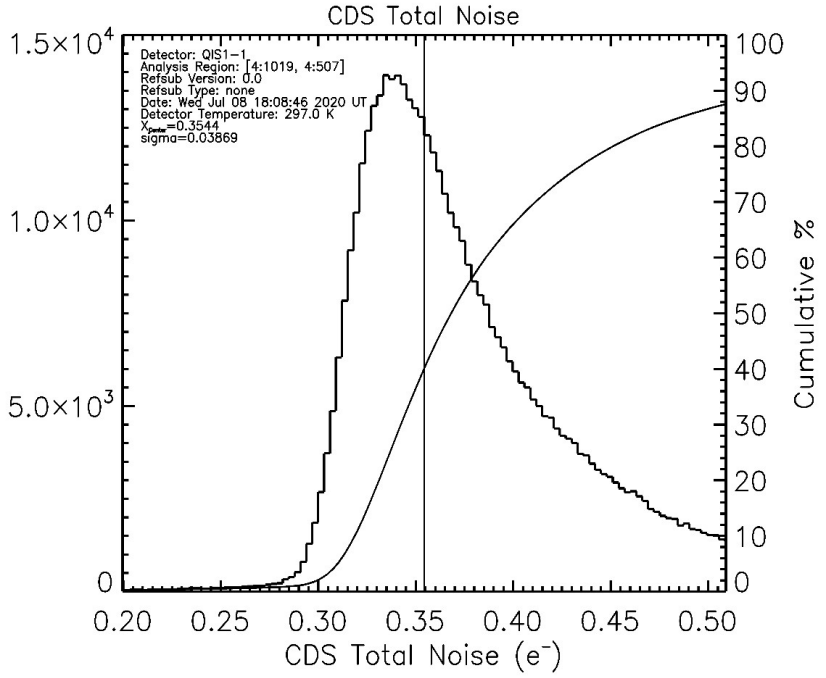

Figure 4.13: histogram of total noise with 8 CDS samples with simultaneous charge transfer

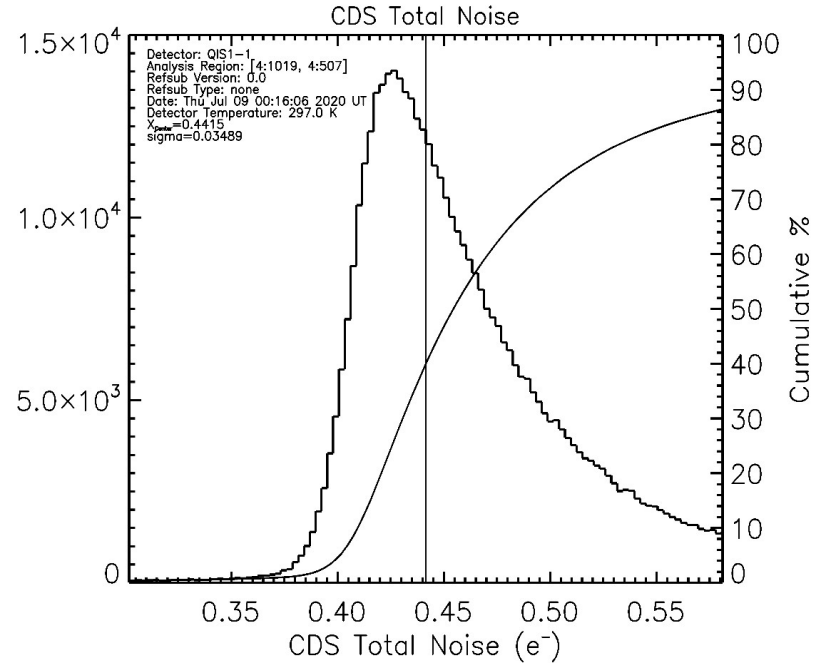

Figure 4.14: histogram of total noise with 4 CDS samples with simultaneous charge transfer

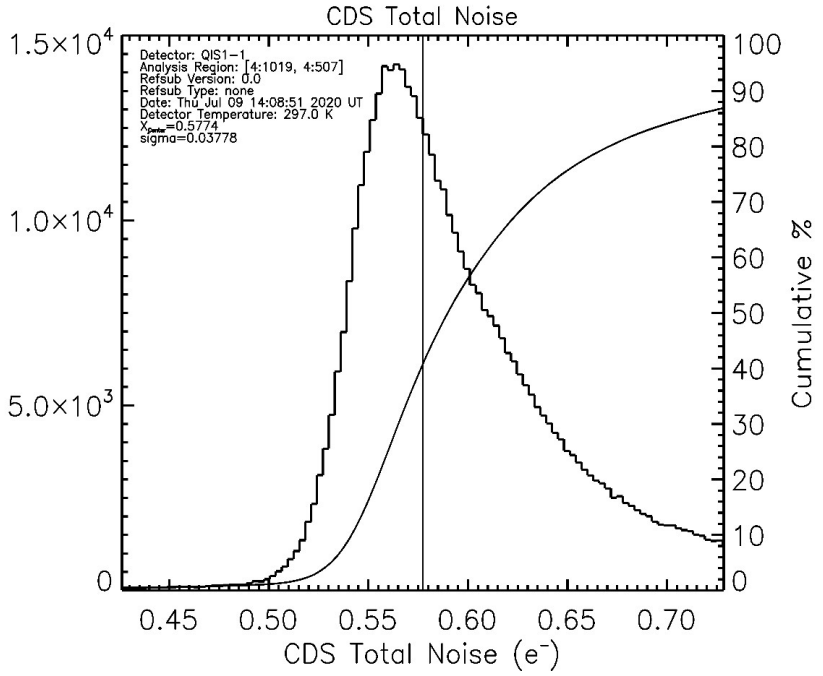

Figure 4.15: histogram of total noise with 2 CDS samples with simultaneous charge transfer

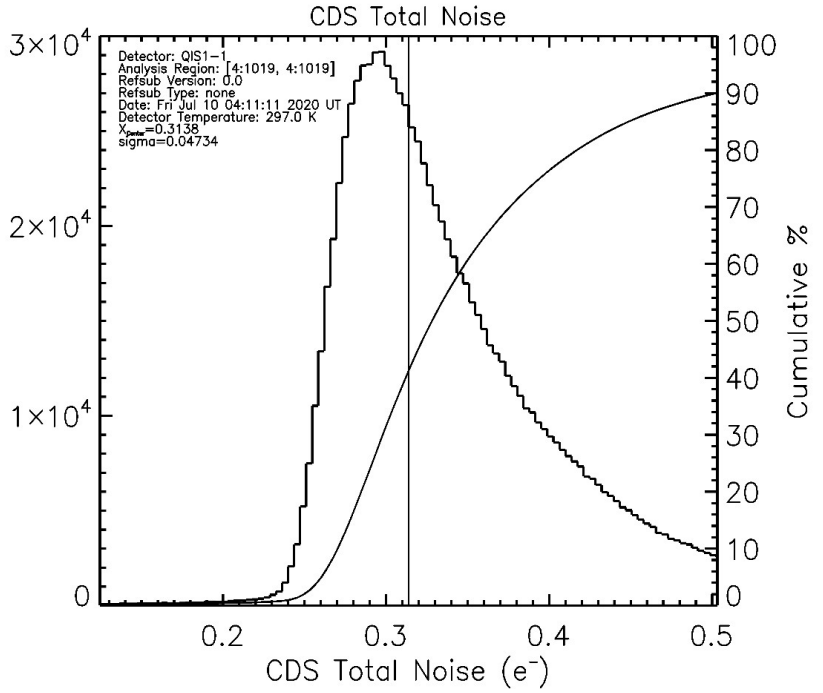

Figure 4.16: histogram of total noise with 16 CDS samples with sequential charge transfer

The total noise of the device is dependent upon the number of CDS samples to average and is not dependent on TX1 and TX2 occurring simultaneously or sequentially. The total noise of the QISPF does not follow a standard Gaussian distribution as would be expected from typical image sensors. Instead, the left side of the distribution is very sharp where the right side has a significant tail. The shape of this unusual distribution is seen in the read noise presented in [61]. The reason for the significant sharp onset of noise is not fully understood.

4.5 Charge to Voltage Factor

The charge to voltage factor of an imaging system is typically determined using the photon transfer curve. For a photon number resolving detector, a second alternative approach is used in this thesis. Charge to voltage factor in this paper is evaluated from two different experiments. The first experiment directly measures the ADC output response for a single electron [ADU/e^-]. The second experiment directly measures the ADC output response for a change in input reset voltage [µV/ADU]. Multiplying both values together with compute the charge to voltage factor of the system.

4.5.1 ADC Conversion Gain

4.5.1.1 Measurement Procedure

ADC conversion gain is evaluated by exposing the image sensor to light and measuring the average spacing between photon-number peaks in a histogram of a pixels output. As the fundamental electron charge is quantized, a histogram of multiple measurements from a pixel will show discrete peaks at each integer number of measured electrons.

The image sensor is placed in a light environment where each pixel measures an average signal of 1 - 5 e^-/pix. The image sensor captures a total of 50,000 frames of data at a constant illumination. A histogram of each pixels output reveals the peaks corresponding to each photon-number. The amplitude of each peak is governed by the Poisson nature of the random arrival time of photons. For each pixel, IDL fits a Gaussian to each peak to evaluate the peak location. This process fits each photon peak and then remove the peak from the data

set. This is important as read noise causes overlap between photon number peaks. The IDL procedure starts on the left side and move right to fit and remove every peak from the data. To prevent a bias from moving left to right, the entire process occurs again by fitting each peak from the right to left. The mean location is computed between both left and right scans. The average distance between the computed mean peak location is the ADC conversion gain. IDL computes the ADC conversion gain for each pixel and plots a histogram of all pixel's ADC conversion gain.

4.5.1.2 ADC Conversion Gain Results

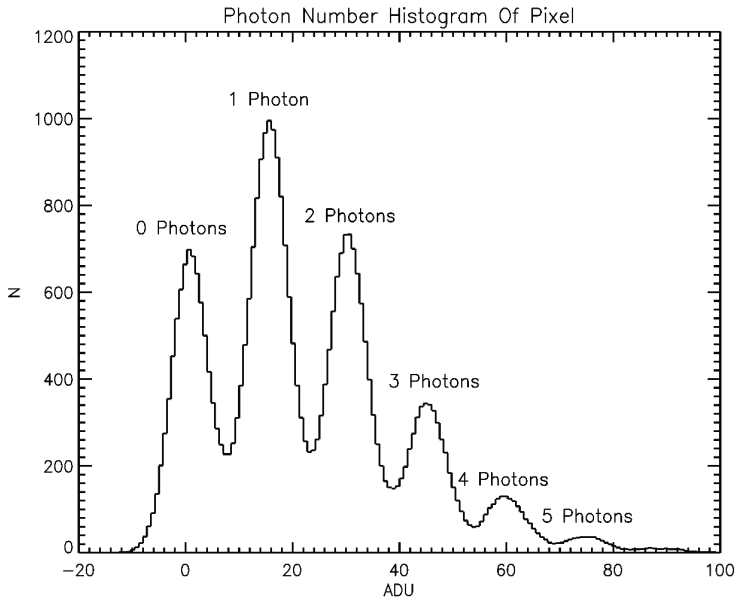

Figure 4.17: photon number resolution histogram of a single pixel

Figure 4.17 demonstrates the photon number resolution capability for a single pixel in the detector array. The pixel resolves individual photons that are measured from the CDS readout. This data was creating using 50,000 measurements of a single pixel performing 16 CDS samples. This pixel has an ADC conversion gain of approximately 15 [ADU/e^-] as each photon number peak is located at a multiple of 15 ADU. Almost all pixels in the detector array demonstrate resolved peaks for each photon number. A small number of pixels in the detector array have

a heightened read noise as demonstrated by the long tail in figure 4.12. This prevents the evaluation of photon number resolution for those pixels.

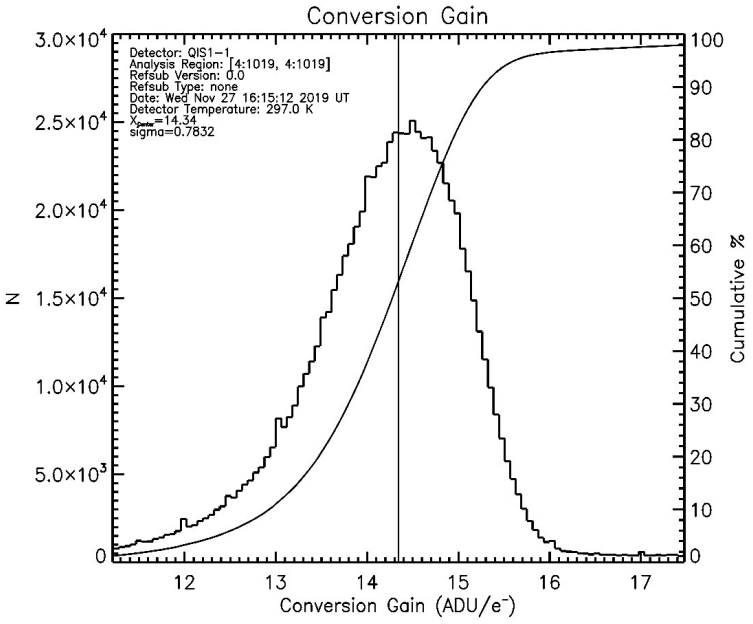

Figure 4.18: histogram of the computed ADC conversion gain for the detector array

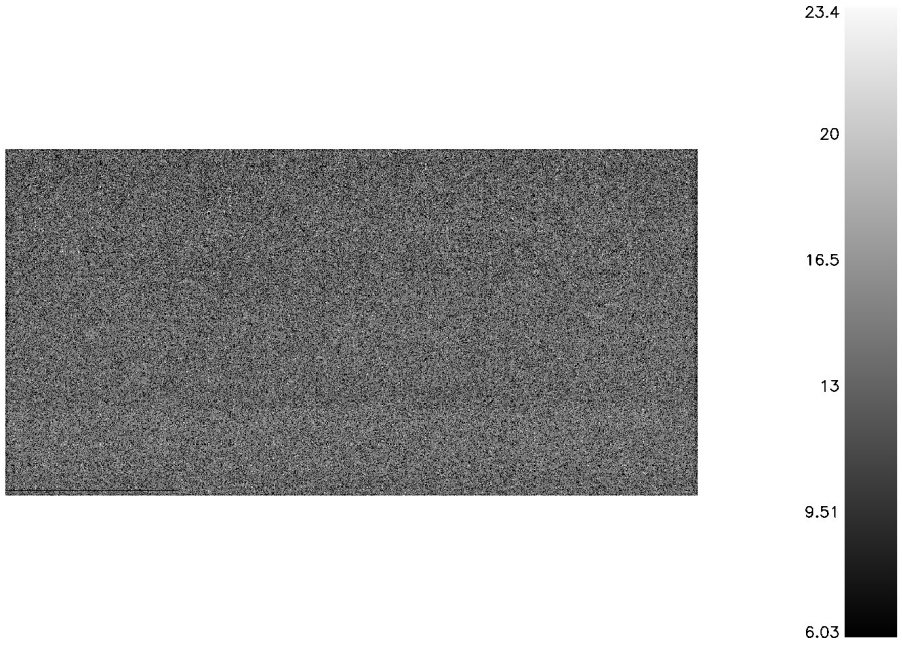

Figure 4.19: map of computed ADC conversion gain [ADU/e$^-$] for the detector array

The mean ADC conversion gain for the detector array is evaluated from an Gaussian fit to the distribution of calculated conversion gain. The mean ADC conversion gain is measured as 14.34 [ADU/e^-]. Research is being performed to determine if the large tail on the left side of figure 4.18 is due to the behavior of the detector array or is due to how the IDL procedure fits peaks. The pixels that appear to have a lower ADC conversion gain do not appear to have a pattern in the detector array as seen in figure 4.19.

4.5.2 Electronic Gain

4.5.2.1 Measurement Procedure

Electronic gain of a pixel is evaluated as the linear slope of the ADC average CDS reset output as a function of the reset voltage. A Gaussian fit to a histogram of all computed electronic gains evaluates the detectors average electronic gain.

IDL procedures place the image sensor in a dark environment and varies the reset voltage of the FD and photodiode between 1.6 V - 2.0 V. The QISPF captures 1000 frames of data per reset voltage and IDL averages each pixel's measurements. The average ADC reset value of a pixel is plotted as a function of FD reset voltage where a linear slope calculates the electronic gain for that pixel. A histogram of electronic gain for all pixels determines the average electronic gain for the entire detector array.

4.5.2.2 Electronic Gain Results

The electronic gain is measured to be 34.7 µV/ADU as the average of the entire detector array (figure 4.20). As you can see from figure 4.21, the histogram of calculated electronic gain for all pixels is a very narrow distribution with a width of 3.37 µV/ADU. Due to sectioning the detector array into clusters with dedicated readouts as described in section 1.4.2, rows of clusters that share an ADC have a similar electronic gain, but, deviates when comparing clusters connected to different ADCs (figure 4.22).

A challenge of the QISPF is that it is not possible to directly measure the reset voltage after the source follower. The QIS chip contains a pad that allows for the direct measurement

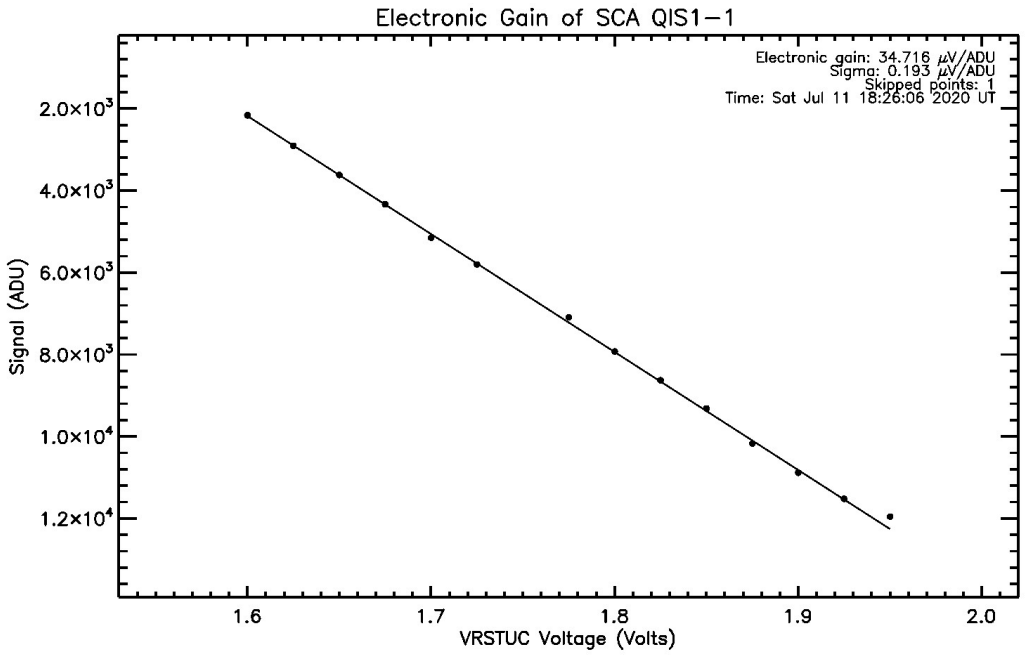

Figure 4.20: average detector array reset signal with electronic gain slope of 34.7 µV/ADU

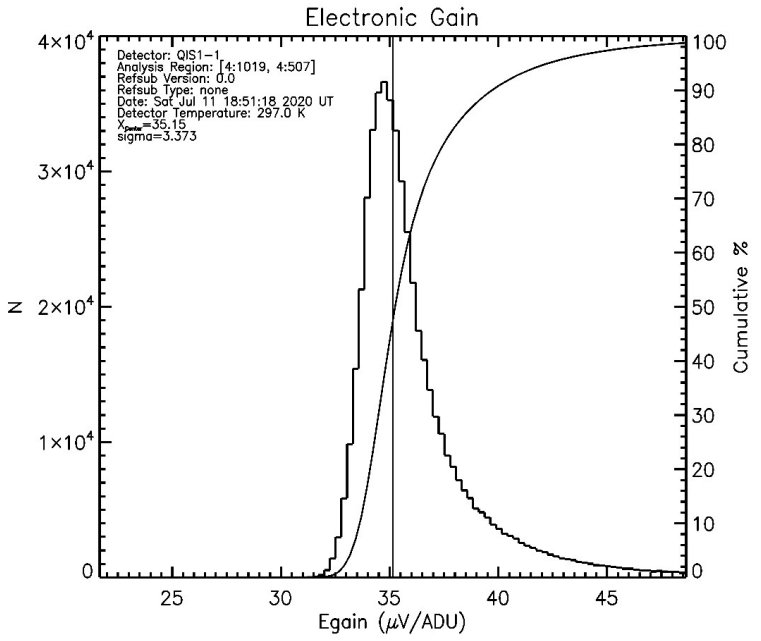

Figure 4.21: histogram of electronic gain for detector array

of the column select located after the SF, however, this pad is not wire-bonded to a lead on the chip carrier. Instead, the reset voltage is taken from the input voltage IDL sets the DAC

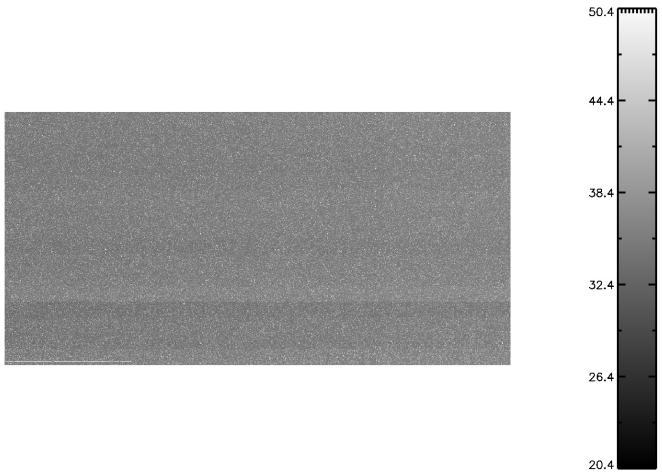

Figure 4.22: map of electronic gain [µV/ADU] for simultaneous TX

to on the PCB. This makes two assumptions: i) the DAC is ideal and will output a voltage exactly the same as the input digital value; ii) the reset FET is ideal and causes no degrade of the reset voltage across the FET.

4.5.3 Charge to Voltage Factor Analysis

The mean ADC conversion gain is 14.3 [ADU/e^-]. The mean electronic gain is 34.7 µV/ADU. Together, the mean charge to voltage factor is 497 µV/e^-. This charge to voltage factor is higher than published values ([32]) and is due to not being able to directly measure the output-referred reset voltage after the SF. Typical SFs for CMOS active pixel sensors have a gain between 0.5 and 0.9 [62]. Considering this, the charge to voltage factor will decreases to a value closer to published charge to voltage factors.

4.6 Leakage Current Effect

Comparing the QISPF response to a calibrated diode and discussion with Dartmouth College outlined that that leakage current across TX was a significant effect. Leakage current affects the evaluation of quantum efficiency and is the culprit for the unusual non-linear dark current found in sequential charge transfer of TX and integration times greater than 2 s. While future

designs can mitigate this effect, it became apparent that the work performed during this thesis would have to consider leakage current in each measurement.

To evaluate the effect of leakage current on the single-photon counting capability of the QISPF, a Fiber-Lite MI-150 high intensity illuminator replaced the monochromator as it can achieve a wide range of light intensity. The MI-150 is manually adjusted with a linear knob to output different intensities of light from a knob of 0% to 100% power. The optical fiber of the MI-150 is positioned at the entrance of the integration box. An experiment was performed that would measure the average of 10 frames from the QISPF with TX occurring sequentially as a function of the average of 10 measurements of a calibrated Gooch and Housego silicon diode. The diode has been calibrated by Gooch and Housego twice over the last decade and is utilized to perform a system calibration of the integrating box for quantum efficiency.

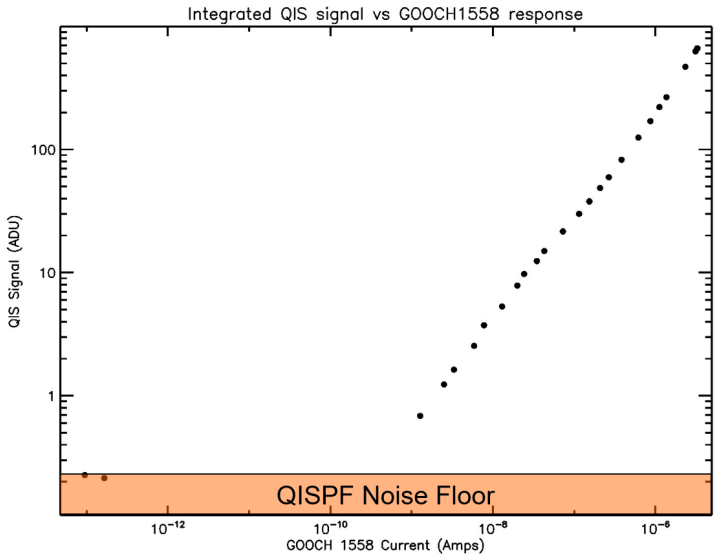

Figure 4.23: QISPF measured signal as a function of calibrated silicon diode

During the experiment, the adjustable light source was varied by adjusting the knob to different power settings and allowed to rest for five minutes to reach a stable temperature. Unfortunately, The MI-150 knob is not precise enough to allow a light intensity that the calibrated diode would measure a current between $10^{-11} - 10^{-9}$ A. While the calibrated diode measures very small intensities of light, figure 4.23 demonstrates that leakage current prevents the QISPF outputting a signal above the noise floor of approximately 0.1 ADU. The QISPF

would not output a noticeable response until the calibrated diode would measure a current 10^{-9} A. Using the calibrated spectral response of the diode, a current of 10^{-9} A corresponds to an intensity of $2 \cdot 10^{-9}$ W. The QISPF measures an average of one e^-/pix or 15 ADU/pix when the calibrated diode measured a current of 10^{-7} A or $2 \cdot 10^{-7}$ W. An order of magnitude expected output of the QISPF (equation 4.6.1) can be computed by assuming the $2 \cdot 10^{-7}$ W is solely comprised of 500 nm photons. I derived the equation below to compute the number of expected photons:

$$N_{\text{pho}} = \frac{P}{hc/\lambda} \cdot \frac{A_{\text{pix}}}{A_{\text{d}}} \cdot t_{\text{int}} \cdot QE \tag{4.6.1}$$

where N_{pho} is the number of photons, P is the total power of incident light, λ is the wavelength of light, A is the area of the pixel (pix) and diode (d), t_{int} is the integration time, and QE is the quantum efficiency of the QISPF.

For a measured power of $2 \cdot 10^{-7}$ W, the QISPF should measure approximately two hundred electrons. Instead the QISPF only measures a single electron at this intensity. While the QISPF is photon number resolving, the difference in the calibrated diode measured intensity of light and the QISPF response identifies an issue with the single photon sensing ability of the analog QIS detector described in this work. While the digital QIS devices are not characterized in this work, they have been published to operate at full-frame readout speeds greater than 1 kHz. The analog QIS in this work will readout the entire array in 0.6 - 9.6 fps. This is due to the utilization of an off-chip ADC. With a multi-bit ADC integrated on chip, the QISPF in this thesis could readout much faster, significantly reducing the time for leakage current, benefiting the single-photon sensing ability of multi-bit QIS devices.

The effect of leakage current was further evaluated as a function on integration time from the average reset samples before the subtraction in CDS. An IDL procedure sets the light level to when the QISPF measures an average of $0.40 e^-$/pix. The experiment consists of capturing the average reset sample for 25 frames for a range of integration times.

Comparing figure 4.24 and figure 4.25, even though the QISPF measures an average CDS signal of 0.40 e^-/pix, the leakage current is significantly greater than a single electron. After

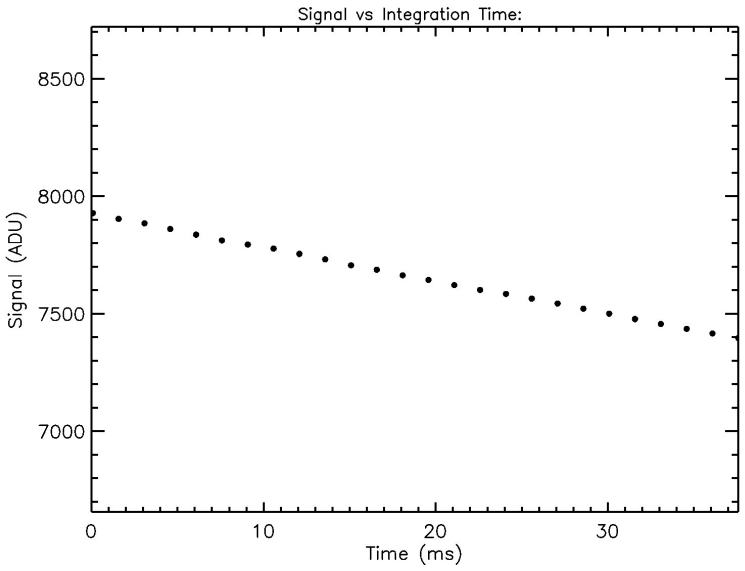

Figure 4.24: average reset sample in dark environment as a function of integration time

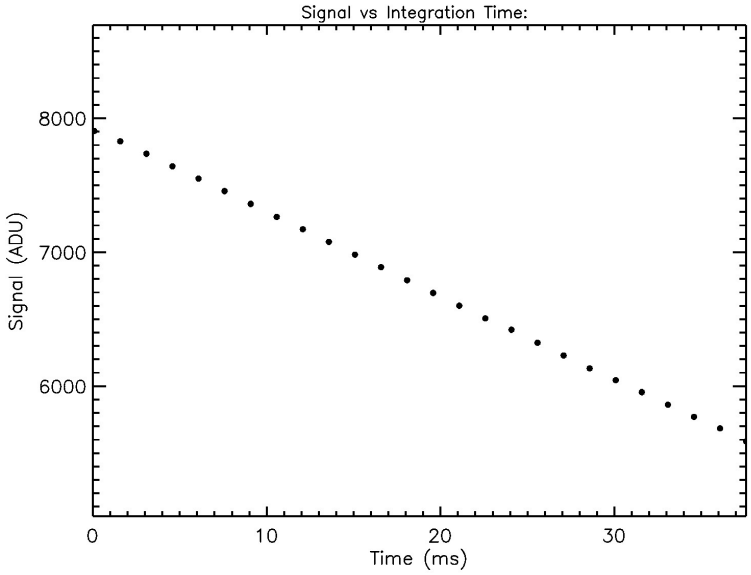

Figure 4.25: average reset sample with CDS measured average signal of 0.40 e^-/pix as a function of integration time

38 ms, the average reset for no incident light is 7400 ADU while the average reset under illumination is 5600 ADU. In section 4.5.1.2, the average ADC conversion gain of detector array is approximately 14.3 ADU/e^-. This corresponds to a difference of 1800 ADU or 125 e^- of leakage current over an integration of 38 ms. Recalling from figure 4.23 that the QISPF

should measure approximately 200 e^- when it outputs a CDS signal measurement of 1 e^-, it is clear that leakage current is an effect that creates major challenges for the single photon sensing of analog QIS devices using an off-chip ADC.

4.7 Quantum Efficiency

Quantum efficiency is evaluated for the entire detector array. The quantum efficiency is computed as the ratio of the average number of electrons generated in the pixel to the average number of incident photons on the pixel during exposure. Quantum efficiency is measured using the calibrated detector method where a calibrated detector will measure the incident number of photons.

4.7.1 Measurement Procedure

Quantum efficiency is a wavelength-dependent measurement, so a monochromator is necessary for this experiment. Quantum efficiency at each wavelength is computed as the average signal measured for all pixels divided by the average signal as measured by a calibrated Gooch and Housego silicon diode. The silicon diode measures the current response and uses a previously calibrated spectral response by Gooch and Housego to compute the number of photons measured.

Quantum efficiency starts with a system calibration scan using two diodes, the Gooch and Housego silicon diode and a second calibrated Scitech silicon diode. The Gooch and Housego is referred to as the "Calibrated Diode" and the Scitech is referred to as the "Monitoring Diode". To perform a system calibration, the calibrated diode replaces the QISPF while the monitoring diode remains in the same location during system calibration and the quantum efficiency experiment. The goal of the system calibration is to measure the incident light at the detector with a calibrated diode and create a text file that represents the calibration of the integration box at the location of the detector. This is shown in figure 4.26. During the quantum efficiency experiment, the monitoring diode measures any possible variation in the light intensity between experiments to adjust the QISPF measured signal so that it can be

divided by the calibrated diode measurement.

The detector and monitoring diode will scan a wavelength range of 200 nm to 1200 nm, which spans the photosensitive range for a silicon detector. The monochromator is set to have a slit width of 3000 µm corresponding to a bandpass of roughly 10 nm. As such, the monochromator will perform a scan of the wavelength range with a resolution of 5 nm.

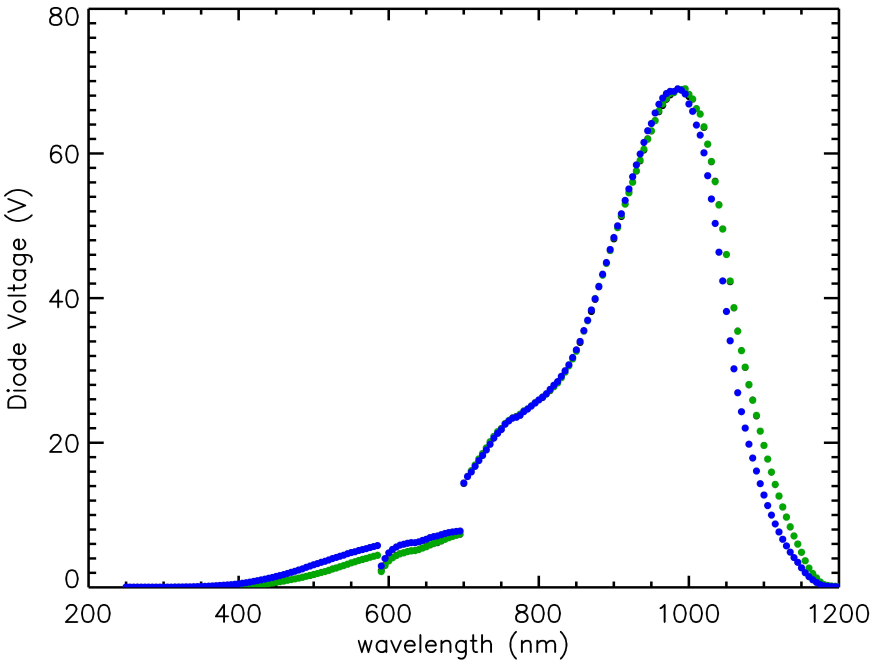

Figure 4.26: spectral response scan of monitoring diode (blue) and calibrated diode (green)

At each wavelength, the QISPF performs four different measurements and the monitoring diode will perform two different measurements. The QISPF captures 1000 frames of data for each different type of measurement where the monitoring diode will simultaneously perform two sets of measurements with 10 samples per measurement. The QISPF will perform two measurements while the filter wheel is closed, one at an integration time of 20 ms and the other at 25 ms. At the same time, the dark environment will be sampled multiple times by the monitoring diode. After this, the filter wheel is then set to allow light to enter the monochromator. However, the filter can change between wavelength steps to prevent unwanted higher order wavelengths of light from entering the integrating box. Once again, the QISPF performs two sets of measurements with integration times of 20 ms and 25 ms. At the same

time, the monitoring diode will sample the flux in the integrating box.

4.7.2 Quantum Efficiency Results

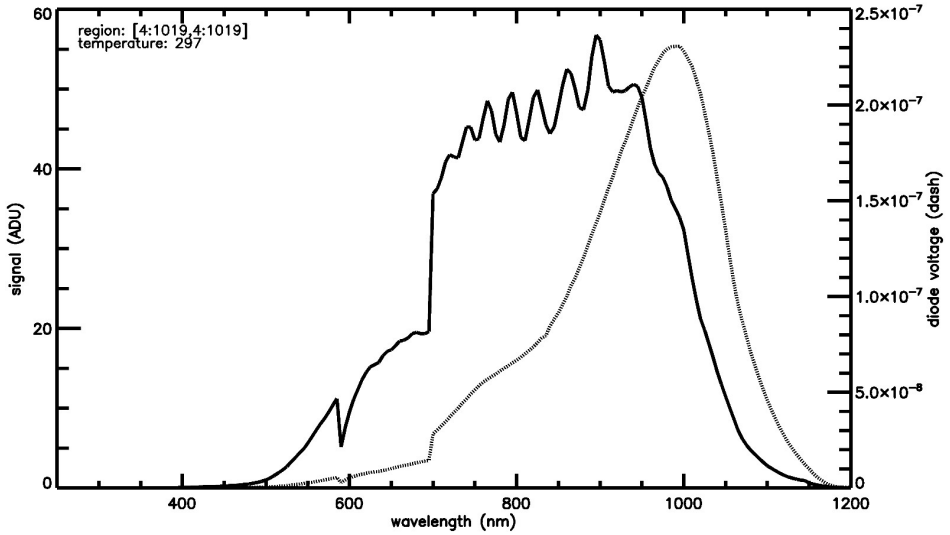

Figure 4.27: response of the QIS signal (solid line) and measured current of calibrated diode (dash line)

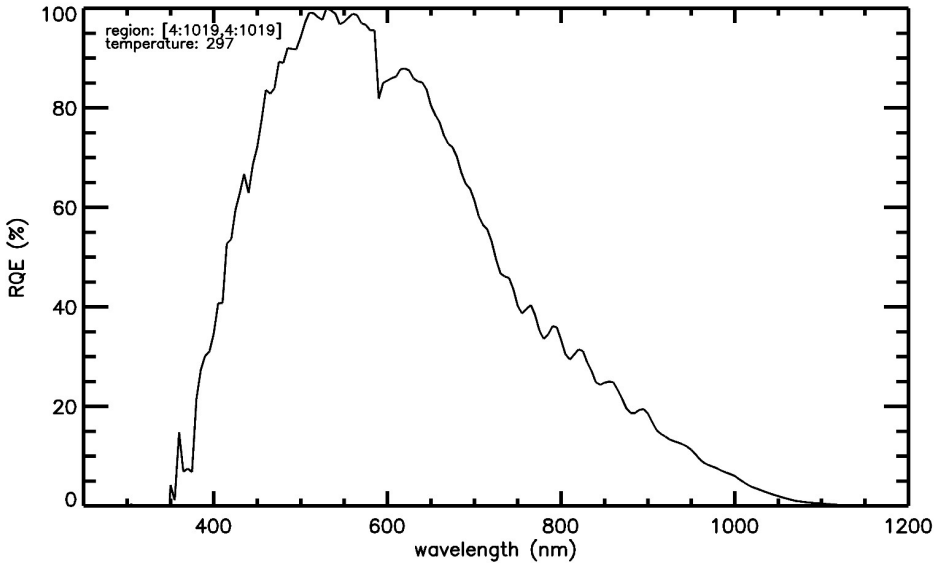

Figure 4.28: relative quantum efficiency

Figure 4.27 demonstrates the challenge that leakage current provides for calculating abso-

lute quantum efficiency. For wavelengths below 500 nm, the measured current of the calibrated diode is 10^{-9}A. In section 4.6, this response from the diode corresponds to the start of a noticeable response from the QISPF. The noise floor of the QISPF was measured to be around 0.1 - 0.2 e^- (1.5 - 3.0 ADU). At such a low signal, the signal to noise is reduced at these wavelengths.

At sub-500 nm wavelengths, the relative quantum efficiency curve (figure 4.28) contains sharp features. This is primarily due to measuring quantum efficiency with a CDS signal smaller than the noise floor of the QISPF. If leakage current did not occur over the transfer gate, the expected response of the QISPF would be higher, thus, allowing a valid absolute quantum efficiency to be measured. For wavelengths longer than 500 nm, the quantum efficiency curve does not contain any sharp features that would be a result of poor signal to noise.

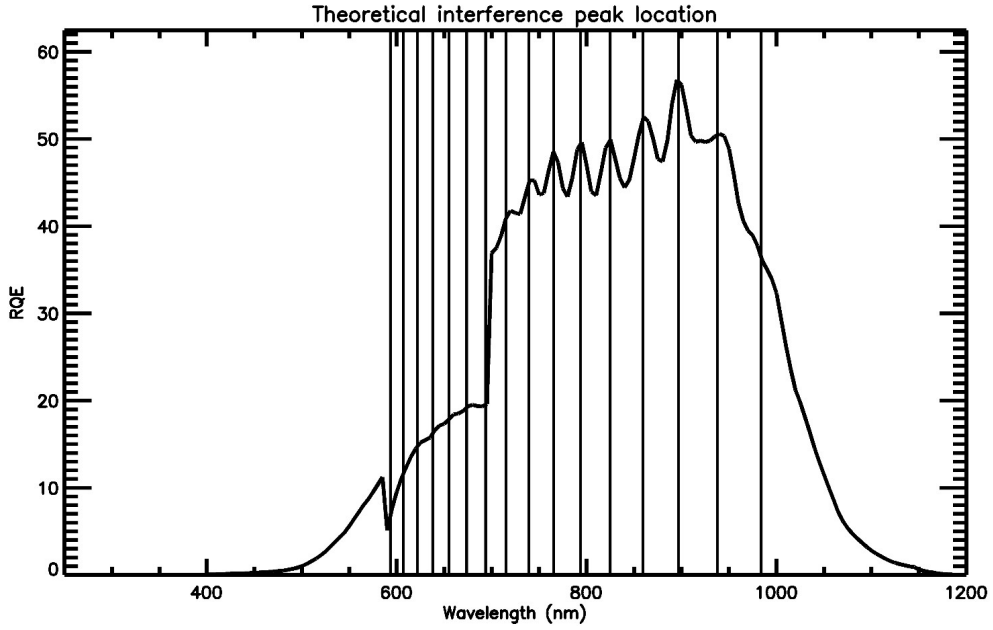

Figure 4.29: theoretical fringe locations for an oxide layer thickness of 2476 nm

As described in section 3.4, fringing from interference due to oxide layers is observed in the quantum efficiency and raw data wavelength scans. This effect is very apparent in the QISPF relative quantum efficiency curve and the response of the QISPF. An short analysis determines the effective oxide thickness that would cause the fringing. For this analysis, simple thin film

interference equations were used to model the interference for a single oxide layer. The optical reflective index of silicon as a function of wavelength was taken from [63] [64] [65]. An new IDL procedure plotted the theoretical locations of interference peaks. The IDL procedure was run multiple times until the theoretical locations matched the large amplitude fringing found between 700 nm and 900 nm. This occurred for only a single input thickness of 2476 nm.

While a single thin film thickness of 2476 nm (4.29) visually matches the large amplitude fringing, it is clear that the theoretical analysis does not appear to match any smaller amplitude fringing at wavelengths shorter than 700 nm indicating that the fringing may be a result of a more complicated oxide structure. Such a structure would be more apparent with an increased signal response from the QISPF at sub-700 nm.

Chapter 5

Conclusion

Figure 5.1: QISPF image with average of $0.8e^{-}$ per pixel

During my thesis, I implemented the QISPF into the automatic data acquisition and reduction pipeline at the CfD, constructed a test suite for the QISPF, and performed preliminary work for the NASA SAT funded project. My work validated the room temperature photon

number resolution of the image sensor and the published room temperature dark current, total noise, and charge-to-voltage factor (table 5.1). With extensive work mitigating the effects of leakage current, the peak quantum efficiency of 85% at 480 nm was validated, however, a presentable scan over the wavelength response of Silicon was not created and presented in this work as the leakage current is not taken into account in the quantum efficiency pipeline at CfD.

Table 5.1: Summary of QISPF Characterization

Characterization Metric	Value
Dark Current (297 K)	0.028 e^-/s/pix
Total Noise (CDS 16)	0.31 e^-
ADC Conversion Gain	14.7 ADU/e^-
Electronic Gain	35.1 µV/ADU
Effective Charge to Voltage	≈500 µV/e^-

My work identified important considerations and next steps for the SAT funded project moving forward. First, the leakage current across the transfer gate must be further investigated in order to measure an accurate absolute quantum efficiency. To do this, the non-linearity of the QIS must be modeled to allow for the correct calculation in the quantum efficiency analysis IDL procedure. A new test suite would have to be assembled to include a dewar for extensive characterization in a simulated space environment. The QIS device will need to be implemented into more IDL procedures that measure other characterization metrics not demonstrated in this work, such as intra-pixel sensitivity, linearity, crosstalk, and persistence. For intra-pixel sensitivity, the small 1.1 µm pixel will provide a challenge to measure intra-pixel sensitivity using the standard method of scanning the pixel with the 6 µm beam at the CfD. For persistence, a light chopper will be used to allow pulses of light to hit the detector where the persistence of trapped signal can be measured. Considering the rolling shutter of the QIS device in this work, only a small region of the detector array will be operated in this experiment to prevent loss of measured persistence due to leakage current.

The final goal of the SAT project is a redesign of the chip for improved performance based

upon the results of the earlier characterization phases and information obtained by RIT from the astronomy community regarding the most up-to-date version of future detector needs.

For future astrophysical applications, the redesign of the QIS will need to mitigate leakage current, include a global shutter, and increase the frame rate. Leakage current will be mitigated through further prototyping of different detector architecture and doping concentration. The global shutter and frame rate can be addressed by using multi-bit ADCs on chip. It is likely that the pixel size, format size, and output circuit (JFET vs. MOSFET, buried vs. surface channel) will be of particular interest in this redesign. In the case of the output circuit, the SAT project team will be attempting to lower the noise, as opposed to what was done in most of the QIS development effort up until now in increasing the signal.

Bibliography

[1] C. Kouveliotou, E. Agol, N. Batalha, J. Bean, M. Bentz, N. Cornish, A. Dressler, E. Figueroa-Feliciano, S. Gaudi, O. Guyon, D. Hartmann, J. Kalirai, M. Niemack, F. Ozel, C. Reynolds, A. Roberge, K. Sheth. A. Straughn, D. Weinberg, and J. Zmuidzinas. Enduring Quests-Daring Visions (NASA Astrophysics in the Next Three Decades), 2014. 1

[2] E.F. Schubert. *Doping in III-V Semiconductors*. Cambridge Studies in Semiconductor Physics and Microelectronic Engineering. Cambridge University Press, 1993. 1.1

[3] G.P. Weckler. Operation of p-n Junction Photodetectors in a Photon Flux Integrating Mode. *IEEE Journal of Solid-state Circuits*, 2:65–73, 1967. 1.1

[4] R.H. Dyck and G.P. Weckler. Integrated Arrays of Silicon Photodetectors for Image Sensing. *IEEE Transactions on Electron Devices*, 15(4):196–201, 1968. 1.1

[5] E.R. Fossum. Camera-on-a-Chip: Technology Transfer From Saturn to Your Cell Phone. *Technology & Innovation*, 15(3):197–209, December 2013. 1.1

[6] E.R. Fossum, S. Mendis, and S.E. Kemeny. Active Pixel Sensor with Intra-Pixel Charge Transfer, 1995. US Patent 5,471,515. 1.1

[7] E.R. Fossum and R. Nixon. CMOS Active Pixel Sensor Type Imaging System on a Chip, 1998. US Patent 5,841,126. 1.1

[8] T. Inoue, S. Takeuchi, and S. Kawahito. CMOS Active Pixel Image Sensor with In-Pixel CDS for High-Speed Cameras. In N. Sampat, R.J. Motta, and M.M. Blouke, editors, *Sen-*

sors and Camera Systems for Scientific, Industrial, and Digital Photography Applications V, volume 5301, pages 250 – 257. International Society for Optics and Photonics, SPIE, 2004. 1.1

[9] J. Janesick, T. Elliott, J. Andrews, and J. Tower. Fundamental performance differences of CMOS and CCD imagers: part VI. In J.A. Koch and G.P. Grim, editors, *Target Diagnostics Physics and Engineering for Inertial Confinement Fusion IV*, volume 9591, pages 1 – 17. International Society for Optics and Photonics, SPIE, 2015. 1.1

[10] R. Lineback. Nonstop CMOS Image Sensor Sales Records Seen Through 2021, 2017. 1.1

[11] D. Neamen. *Semiconductor physics and devices : basic principles*. McGraw-Hill, New York, NY, 2012. 1.2

[12] J.R. Hook and H.E. Hall. *Solid State Physics*. 07 1995. 1.2

[13] G. Rieke. *Detection of Light: From the Ultraviolet to the Submillimeter*. Cambridge University Press, 08 2020. 1.2

[14] E.R. Fossum and D.B. Hondongwa. A Review of the Pinned Photodiode for CCD and CMOS Image Sensors. *IEEE Journal of the Electron Devices Society*, 2(3):33–43, May 2014. 1.2, 3.3.1

[15] U. Jain. Characterization of CMOS Image Sensor, 2016. thesis. 1.3

[16] E.R. Fossum. Gigapixel Digital Film Sensor (DFS) Proposal. In *Nanospace Manipulation of Photons and Electrons for Nanovision Systems*, pages 1 – 4. The 7th Takayanagi Kenjiro Memorial Symposium and the 2nd International Symposium on Nanovision Science, University of Shizuoka, Hamamatsu, Japan, 2005. 1.4

[17] E.R. Fossum. What to do with sub-diffraction-limit (SDL) pixels?–A proposal for a gigapixel digital film sensor (DFS). *Proc. Of the 2005 IEEE Workshop on Charge-Coupled Devices and Advanced Image Sensors*, 01 2005. 1.4

[18] E.R. Fossum, D-K. Cha, Y-G. Jin, Y-D. Park, and S-J. Hwang. High sensitivity image sensors including a single electron field effect transistor and methods of operating the same. US Patent No. 8,546,901 and 8,803,273. 1.4

[19] E.R. Fossum. The Quanta Image Sensor (QIS): Concepts and Challenges. 07 2011. 1.4

[20] E.R. Fossum. Image Sensor using Single Photon Jots and Processor to Create Pixels, 2006. US Patent 8,648,287. 1.4

[21] Y. Chi, A. Gnanasambandam, V. Koltun, and S.H. Chan. Dynamic Low-light Imaging with Quanta Image Sensors, 2020. 1.4

[22] J. Ma and E.R. Fossum. A Pump-Gate Jot Device With High Conversion Gain for a Quanta Image Sensor. *IEEE Journal of the Electron Devices Society*, 3(2):73–77, March 2015. 1.4.1

[23] J. Ma, D. Starkey, A. Rao, K. Odame, and E. R. Fossum. Characterization of Quanta Image Sensor Pump-Gate Jots With Deep Sub-Electron Read Noise. *IEEE Journal of the Electron Devices Society*, 3(6):472–480, November 2015. 1.4.1

[24] E.R. Fossum, J. Ma, S. Masoodian, L. Anzagira, and R. Zizza. The quanta image sensor: Every photon counts. *Sensors*, 16(8):1260, August 2016. 1.4.1

[25] J. Ma and E.R. Fossum. Analytical Modeling and TCAD Simulation of a Quanta Image Sensor Jot Device With a JFET Source-Follower for Deep Sub-Electron Read Noise. *IEEE Journal of the Electron Devices Society*, 5(1):69–78, 2017. 1.4.1

[26] J. Ma, D. Hondongwa, and E.R. Fossum. Jot devices and the Quanta Image Sensor. In *2014 IEEE International Electron Devices Meeting*, pages 10.1.1–10.1.4, 2014. 1.6

[27] E.R. Fossum, D. Starkey, W. Deng, J. Ma, and S. Masoodian. Quanta imaging sensors: achieving single-photon counting without avalanche gain. In M.S. Islam, A.K. Dutta, and T. George, editors, *Micro- and Nanotechnology Sensors, Systems, and Applications X*. SPIE, May 2018. 1.4.2

[28] W. Deng, D. Starkey, S. Masoodian, J. Ma, and E.R. Fossum. Quanta image sensors: photon-number-resolving megapixel image sensors at room temperature without avalanche gain. In M.A. Itzler and J.C. Campbell, editors, *Advanced Photon Counting Techniques XII*, volume 10659, pages 1 – 8. International Society for Optics and Photonics, SPIE, 2018. 1.4.2

[29] J. Ma, L. Anzagira, and E.R. Fossum. A 1 μm-Pitch Quanta Image Sensor Jot Device With Shared Readout. *IEEE Journal of the Electron Devices Society*, 4(2):83–89, 2016. 1.4.2

[30] R.M. Guidash, R. Mruthyunjaya, and W. Xu. Shared Amplifier Pixel with Matched Coupling Capacitances, 2007. US Patent US7238926B2. 1.4.2

[31] Jiaju Ma, Saleh Masoodian, Tzu-Jui Wang, and Eric R Fossum. Experimental Comparison of MOSFET and JFET 1.1 um Pitch Jots in 1Mjot Stacked BSI Quanta Image Sensors. In *Proceedings of the 2017 International Image Sensor Workshop (IISW), Hiroshima, Japan*, pages 226–229, 2017. 1.4.3

[32] W. Deng, D. Starkey, J. Ma, and E. R. Fossum. Modelling Measured 1/f Noise in Quanta Image Sensors (QIS). *Sensors*, June 2019. 1.8, 3.2.6, 4.5.3

[33] D.C. Wells, E.W. Greisen, and R.H. Harten. FITS - a Flexible Image Transport System. *Astronomy and Astrophysics Supplement*, 44:363, jun 1981. 1.4.3

[34] S. Donati. *Photodetectors: Devices, Circuits, and Applications*. Prentice Hall, Nov 1999. 1.5

[35] V. Goiffon. *Radiation Effects on CMOS Active Pixel Image Sensors*, page 295–332. CRC Press, 11 2015. 2.1

[36] J. Tan, B. Buttgen, and A. Theuwissen. Analyzing the Radiation Degradation of 4Transistor Deep Submicron Technology CMOS Image Sensors. *IEEE Sensors Journal - IEEE SENS J*, 12:2278–2286, 06 2012. 2.1

[37] The LUVOIR Team. The LUVOIR Mission Concept Study Final Report, 2019. 2.1.1

[38] B.J. Rauscher, M.R. Bolcar, M. Clampin, S.D. Domagal-Goldman, M.W. McElwain, S.H. Moseley, C. Stahle, C.C. Stark, and H.A. Thronson. ATLAST detector needs for Direct Spectroscopic Biosignature Characterization in the Visible and Near-IR. In H.A. MacEwen and B. Breckinridge J, editors, *UV/Optical/IR Space Telescopes and Instruments: Innovative Technologies and Concepts VII*, volume 9602, pages 136 – 143. International Society for Optics and Photonics, SPIE, 2015. 2.1.1

[39] H.A. Thronson, M. Clampin, M. Postman, D. Redding, and H.P. Stahl. Continuing the legacy of the hubble space telescope a large-aperture uvoir space telescope, May 2015. 2.1.1

[40] B.J. Rauscher, M.R. Bolcar, M. Clampin, S.D. Domagal-Goldman, M.W. McElwain, S.H. Moseley, C. Stahle, C.C. Stark, and H.A. Thronson. Life Finder Detectors; Detector Needs and Status for Spectroscopic Biosignature Characterization. In *American Astronomical Society Meeting Abstracts #227*, volume 227 of *American Astronomical Society Meeting Abstracts*, page 147.24, January 2016. 2.1.1

[41] S.B. Gaudi et al. The Habitable Exoplanet Observatory (HabEx) Mission Concept Study Final Report, 2020. 2.1.2

[42] H. Nyquist. Certain Topics in Telegraph Transmission Theory. *Transactions of the American Institute of Electrical Engineers*, 47(2):617–644, 1928. 2.4

[43] P. P. Vaidyanathan. Generalizations of the sampling theorem: Seven decades after Nyquist. *IEEE Transactions on Circuits and Systems I: Fundamental Theory and Applications*, 48(9):1094–1109, 2001. 2.4

[44] B.W. Carroll and D.A. Ostlie. *An Introduction to Modern Astrophysics*. Pearson, 08 2020. 2.4

[45] G. Agranov, R. Mauritzson, J. Ladd, A. Dokoutchaev, X. Fan, X. Li, Z. Yin, R. Johnson, V. Lenchenkov, S. Nagaraja, W. Gazeley, J. Bai, H. Lee, D. Anna, and G. De Amicis.

Pixel continues to shrink.... Pixel Development for Novel CMOS Image Sensors. *Proc. IISW*, June 2011. 3.1

[46] N.V. Loukianova, H.O. Folkerts, J.P.V. Maas, D.W.E. Verbugt, A.J. Mierop, W. Hoekstra, E. Roks, and A.J.P. Theuwissen. Leakage Current Modeling of Test Structures for Characterization of Dark Current in CMOS Image Sensors. *IEEE Transactions on Electron Devices*, 50(1):77–83, January 2003. 3.1.1

[47] J.R. Janesick. *Scientific Charge-Coupled Devices*. SPIE, January 2001. 3.1.1

[48] W.C. Porter, B. Kopp, J.C. Dunlap, R. Widenhorn, and E. Bodegom. Dark current measurements in a CMOS imager. In M.M. Blouke and E. Bodegom, editors, *Sensors, Cameras, and Systems for Industrial/Scientific Applications IX*. SPIE, February 2008. 3.1.2

[49] Y. Cao, F. Tang, A. Bermak, and T. Le. A smart CMOS image sensor with on-chip hot pixel correcting readout circuit for biomedical applications. In *2010 Fifth IEEE International Symposium on Electronic Design, Test & Applications*. IEEE, 2010. 3.1.2

[50] D. Durini and D. Arutinov. 2 - operational principles of silicon image sensors. In D. Durini, editor, *High Performance Silicon Imaging (Second Edition)*, Woodhead Publishing Series in Electronic and Optical Materials, pages 25 – 73. Woodhead Publishing, second edition edition, 2020. 3.1.3

[51] B. Mheen, Y-J. Song, and A. Theuwissen. Negative Offset Operation of Four-Transistor CMOS Image Pixels for Increased Well Capacity and Suppressed Dark Current. *Electron Device Letters, IEEE*, 29:347 – 349, 05 2008. 3.1.3

[52] W. Xiaohuan. Noise in Sub-micron CMOS Image Sensors, 2008. dissertation. 3.1.4

[53] S.M. Sze and K.K. Ng. *Physics of Semiconductor Devices*. Wiley-Interscience, Hoboken, N.J, 2007. 3.1.5

[54] H. Tian. Noise Analysis in CMOS Image Sensors, August 2000. 3.2

[55] P Fereyre and G Powell. CMOS Image Sensors are Entering a New Age, Jan 2016. 3.2.2

[56] S. Kar. MOSFET: Basics, Characteristics, and Characterization. In *High Permittivity Gate Dielectric Materials*, pages 47–152. Springer Berlin Heidelberg, 2013. 3.2.3

[57] James R. Janesick. *Photon Transfer*. SPIE, August 2007. 3.3

[58] D.A. Starkey and E.R. Fossum. Determining Conversion Gain and Read Noise Using a Photon-Counting Histogram Method for Deep Sub-Electron Read Noise Image Sensors. *IEEE Journal of the Electron Devices Society*, 4(3):129–135, 2016. 3.3

[59] M.W. Coughlin, R.G. Dekany, D.A. Duev, M. Feeney, S.R. Kulkarni, R. Riddle, T. Ahumada, K. Burdge, A.M. Dugas, C.U. Fremling, G. Hallinan, T.A. Prince, and J. van Roestel. The Kitt Peak Electron Multiplying CCD Demonstrator. *Monthly Notices of the Royal Astronomical Society*, 485(1):1412–1419, Feb 2019. 3.3.1

[60] E.R. Fossum and K. Anagnost. The Quanta Image Sensor (QIS): Making Every Photon Count. *Laser Focus World*, 54(1):39–42, Dec 2018. 3.3.1

[61] J. Ma, S. Masoodian, D. A. Starkey, and E. R. Fossum. Photon-number-resolving megapixel image sensor at room temperature without avalanche gain. *Optica*, 4(12):1474, November 2017. 4.4.2

[62] J. Robinson. CMOS Source Resistance and it's Effects on Source-Follower Gain. `https://www.maximintegrated.com/en/design/technical-documents/app-notes/4/4231.html`, Jun 2008. 4.5.3

[63] Optical properties of silicon. `https://www.pveducation.org/pvcdrom/materials/optical-properties-of-silicon`. Accessed: 2020-07-14. 4.7.2

[64] M.A. Green and M.J. Keevers. Optical Properties of Intrinsic Silicon at 300 K. *Progress in Photovoltaics: Research and Applications*, 3:189 – 192, 1995 1995. 4.7.2

[65] M.A. Green. Self-consistent Optical Parameters of Intrinsic Silicon at 300 K including Temperature Coefficients. *Solar Energy Materials and Solar Cells*, 92:1305–1310, 2008. 4.7.2